The precipitating cloud population of the Madden-Julian Oscillation over the Indian and west Pacific Oceans

Hannah C. Barnes[1] and Robert A. Houze Jr.[1]

Received 1 November 2012; revised 27 February 2013; accepted 27 March 2013; published 9 July 2013.

[1] The variability of the precipitating cloud population of the Madden-Julian Oscillation (MJO) is represented by statistics of echo features seen by the Tropical Rainfall Measuring Mission's Precipitation Radar over the central Indian and west Pacific Oceans. Echo features include isolated shallow echoes, deep convective cores, wide convective cores, and broad stratiform regions. Isolated shallow echoes are ever present but most numerous during suppressed MJO phases. Broad stratiform regions dominate variability in areal coverage and maximize during active phases. Deep convective and wide convective cores are more common and variable in number than broad stratiform regions. The magnitude of variability is similar in both regions. In the central Indian Ocean, active MJO phases have synchronous maximization of deep convective entities. In the west Pacific, broad stratiform regions maximize prior to wide convective cores. Reanalysis indicates that isolated shallow echoes are most numerous in dry mid-tropospheric conditions and strong low-level (1000–750 hPa) shear. Mid-tropospheric moisture increases before deeper convective features increase in number, maximizes as deep convective features maximize, and decreases as wide convective cores and broad stratiform regions decline in population. Active-stage deep and wide convective cores occur preferentially with moist mid-tropospheric conditions and strong low-level shear. Acute shear may favor downdraft momentum transport and consequently more robust gust-front convective triggering. Broad stratiform regions maximize with a moist mid-troposphere, strong low-level shear, and moderate upper-level (750–500 hPa) shear that is not so strong that the stratiform region disconnects from its convective moisture source.

Citation: Barnes, H. C., and R. A. Houze Jr. (2013), The precipitating cloud population of the Madden-Julian Oscillation over the Indian and west Pacific Oceans, *J. Geophys. Res. Atmos.*, *118*, 6996–7023, doi:10.1002/jgrd.50375.

1. Introduction

[2] The Madden-Julian Oscillation (MJO) dominates intraseasonal (30–90 day) variability in the equatorial belt [*Madden and Julian*, 1971, 1972]. While upper-level circulation anomalies circumnavigate the globe, the MJO is most readily identifiable as a combined Kelvin and Rossby wave [*Gill*, 1980] that often becomes convectively coupled in the central Indian Ocean, propagates into the west Pacific Ocean, and loses its convective coupling near the date line. When the MJO is convectively coupled, the large-scale atmospheric circulation and convective population reinforce each other. The large-scale circulation provides a favorable environment for convective development, and the latent heat released from the convection strengthens the large-scale circulation [*Lindzen*, 1974]. Even though the coupled convective and circulation anomalies directly linked to the MJO are spatially limited to the equatorial belt in the eastern hemisphere, the MJO influences weather and climate over the globe [*Zhang*, 2005]. Given these teleconnections, an improved understanding of the MJO is expected to benefit global mid- and long-range forecasts.

[3] The convective coupling that occurs over the central Indian and west Pacific Oceans is not well understood, and a first step to improving this knowledge is to accurately describe the changes in the makeup of the convective population as it morphs from shallow fair weather convective clouds into a population that includes deep cloud systems that link with the large-scale circulation of the MJO. Some of the largest members of the population are mesoscale convective systems (MCSs) [*Houze*, 2004], whose precipitating regions cover at least 100 km in horizontal dimension and typically contain a population of deep convective elements along with relatively large stratiform rain areas. The importance of MCSs to the tropical cloud population was noted when *Houze and Cheng* [1977] and *Cheng and Houze* [1979] studied convection in the eastern tropical Atlantic and found that, while convective-scale precipitation radar echoes were far more numerous than mesoscale echoes, a little over 40% of the rainfall was associated with the relatively few mesoscale radar echoes. A global analysis by *Yuan and Houze* [2010] showed active MCSs to be associated with 56% of tropical precipitation. We might therefore expect the MJO to exhibit a higher proportion of MCSs within its

[1]Department of Atmospheric Sciences, University of Washington, Seattle, Washington, USA.

Corresponding author: H. C. Barnes, Department of Atmospheric Sciences, University of Washington, Box 351640, Seattle, WA 98195, USA. (hannah@atmos.washington.edu)

©2013. American Geophysical Union. All Rights Reserved.
2169-897X/13/10.1002/jgrd.50375

convectively coupled active stage than during its suppressed stage. This expectation is consistent with studies using satellite observations of outgoing long-wave radiation [*Mapes and Houze*, 1993; *Chen et al*., 1996], radar data from the Tropical Ocean/Global Atmosphere Coupled Ocean-Atmosphere Response Experiment (TOGA-COARE) [*DeMott and Rutledge*, 1998; *Yuter and Houze*, 1998; *Kingsmill and Houze*, 1999; *Houze et al*., 2000], A-Train satellite data [*Riley et al*., 2011; *Del Genio et al*., 2012; *Yuan and Houze*, 2012], and Tropical Rainfall Measuring Mission (TRMM) satellite products [*Lin et al*., 2004; *Benedict and Randall*, 2007; *Lau and Wu*, 2010]. *Morita et al*. [2006], *Tromeur and Rossow* [2010], and *Del Genio et al*. [2012] found sporadic deep convection to be present during all stages of the MJO. However, we expect the relative frequency of occurrence of such deep convection to vary strongly from one phase of the MJO to the next. Analyzing ship-borne radar data from the *R/V Vickers* during TOGA-COARE, *DeMott and Rutledge* [1998] found that while the variability in the height of the 30 dBZ reflectivity contour, which is used to represent deep intense convection, is small between the convectively enhanced and suppressed stages of the MJO, these intense convective cells contributed proportionally less to the observed rainfall during active stages of the MJO when stratiform precipitation is more prevalent, consistent with the increased role of MCSs during the active phases. *Lin et al*. [2004] showed that 60% of the anomalous precipitation associated with the MJO is linked to the stratiform portion of MCSs. This increased stratiform coverage during the active stage of the MJO is important since it is a signature of a more top-heavy heating profile [*Houze*, 1982, 1989]. Since MCSs constitute the large end of the size spectrum of convective clouds, we focus here on how the cloud population of the MJO evolves in suppressed phases from having few MCSs to active phases hosting numerous MCSs.

[4] Despite the importance of MCSs, it should be kept in mind that these large convective systems only account for about half of the tropical precipitation. Observational and modeling studies have led some to hypothesize that the cloud population systematically transitions from shallow cumulus to cumulus congestus to MCSs as the MJO transitions from its convectively suppressed to convectively active stage as detrainment from convective clouds systematically increases the depth of the moist layer [e.g., *Bladé and Hartmann*, 1993; *Benedict and Randall*, 2007; *Stephens et al*., 2004]. However, whether shallower cumulus clouds are the proximate cause of the moistening and subsequent increasing convective depth remains a matter of debate since large-scale motions may also lead to changes in humidity. Further observational and modeling studies are needed to understand the interaction between shallow cumulus and the environmental moisture field. Regardless of this debate, it will be important to understand how all elements of the convective cloud population (small, medium, and large) vary by phase of the MJO. We therefore assess the makeup of the cloud population in this study by analyzing radar data from the Tropical Rainfall Measuring Mission Precipitation Radar (TRMM PR) [*Kummerow et al*., 1998]. We proceed by taking a census of four echo entities that represent different stages of convective development and, from this census, determining how the composition of the cloud population defined by the frequency distributions of these entities varies from one phase of the MJO to the next.

[5] We further examine the results of the radar echo census in light of the environmental conditions prevailing in each phase of the MJO. Analyses of synoptic-scale conditions within the MJO have previously shown that the variations in the precipitating cloud population coincide preferentially with certain large-scale atmospheric conditions. For example, *Lin and Johnson* [1996], *Chen et al*. [1996], and *Lin et al*. [2004] show that the precipitation maximum associated with the MJO in the west Pacific Ocean occurs roughly 1–3 weeks prior to the westerly wind burst (WWB), 5–10 days before low-level (1000–800 hPa) shear and upper-level (700–150 hPa) shear maximize, and 2–5 days before the highest relative humidity at 600–200 hPa.

[6] General circulation models (GCMs) using conventional cumulus parameterizations struggle to accurately represent the MJO. *Zhang* [2005] pointed out that even when models are able to accurately produce the scale and propagation of the MJO, the period and structure are often unrealistic. However, simulations improve when the cumulus parameterization is altered to allow low-level moisture to build up when the planetary boundary layer is thin [*Takioka et al*., 1988] or when the GCM is superparameterized [e.g., *Randall et al*., 2003; *Benedict and Randall*, 2009]. The latter runs at a course resolution and replaces the cumulus parameterization with a 2-D cloud resolving model. Recent advancements in computing technology increase the resolution of short-term MJO simulations with the GCM running as a fully global cloud resolving model (GCRM). Such a model explicitly simulates the circulation associated with convective entities embedded in the MJO. *Miura et al*. [2007] demonstrated that a realistic MJO could be generated in a GCRM with a 3.5 and 7 km grid resolution. *Benedict and Randall* [2009] and *Miura et al*. [2007] argue that GCM simulations of the MJO are more accurate when the cumulus parameterization is removed since the convection and large-scale circulation can interact in a direct and natural manner.

[7] The interaction between the large-scale atmospheric circulation and convective population as well as its importance with respect to the MJO has been investigated by several numerical modeling studies. *Wu* [2003] found that the heating by shallow convection was necessary to create sufficient low-level moisture convergence to sustain convection on intraseasonal time scales. *Haertel et al*. [2008] found that the MJO is not only sensitive to the deep heating and circulation anomalies produced by deep convection and stratiform regions but also that the shallow heating and upper-level cooling resulting from shallow cumulus and congestus are also important. Their results indicate that the relative amounts of shallow clouds, deep convective elements, and stratiform precipitation are important in determining heating profiles associated with the clouds in the MJO. Consistent with this view, *Zhang and Song* [2009] found that a realistic MJO would not develop without shallow convection even with deep convection accurately represented. Even though models are sensitive to the nature of the cloud population and its interaction with the large-scale atmospheric conditions, the exact relationship among these features is unknown. Thus, a first step to aid development of the model representation of clouds in the MJO is to provide detailed observations of the members of the cloud population and its concurrent large-scale environment in each phase of the MJO.

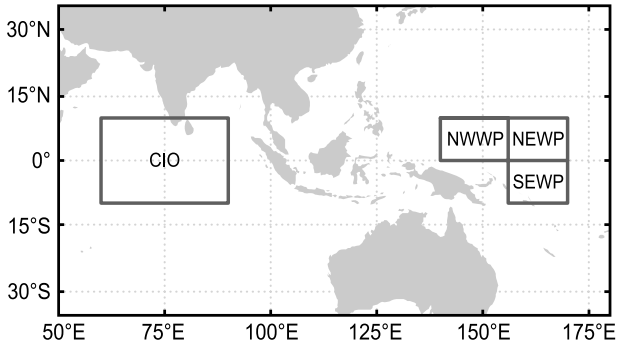


Figure 1. Physical map of the geographic regions analyzed. The central Indian Ocean (CIO) extends from 10°S–10°N, 60°E–90°E. The northwestern portion of the west Pacific Ocean (NWWP) extends from 0°–10°N, 140°E–156°E and includes the warm pool. The northeastern portion of the west Pacific Ocean (NEWP) extends from 0°–10°N, 156°E–170°E and includes the cold tongue. The southeastern portion of the west Pacific Ocean extends from 10°S–0°, 156°E–170°E and includes the South Pacific Convergence Zone (SPCZ).

[8] *Yuan and Houze* [2012] used A-Train satellite data to analyze the variability of large, mature MCSs in the eastern Indian Ocean, Maritime Continent, and west Pacific Ocean with phase of the MJO and related these changes to large-scale conditions indicated by ERA-interim reanalysis. Connected MCSs, which are very large systems, consisting of at least two MCSs joined by precipitation, and often having a thick cloud deck that efficiently produces stratiform precipitation, experience the greatest variability with phase of the MJO. While MODIS brightness temperature data indicate that the depth of convection varies little with phase of the MJO, brightness temperature data are incapable of accurately distinguishing between different types of deep convection. This limitation is resolved in the current study through the use of the TRMM PR data, which successfully separate stratiform from convective rain, isolate the tallest and widest components of deep convection, and identify small, shallow convection. The purpose of this study is to use the capability of the TRMM PR data to characterize the precipitating cloud population of the MJO via these echo types and to relate the evolution of the cloud population to the large-scale environment conditions that change from one MJO phase to the next. Specifically we will:

[9] 1. Determine how the relative amounts of clouds in different stages identified by the TRMM PR change as a function of MJO phase.

[10] 2. Compare the TRMM PR echo population in the Indian Ocean, where many MJOs often become convectively coupled, with the west Pacific, where the MJO more typically moves through as a fully developed disturbance.

[11] 3. Frame observed changes in the precipitating cloud population in context of the large-scale relative humidity fields, circulation patterns, and vertical wind shear conditions associated with each phase of the MJO in both the central Indian Ocean and west Pacific by using global reanalysis coinciding with the TRMM PR data.

2. Data and Methodology

[12] This study uses version 6 of the TRMM Precipitation Radar data obtained over the central Indian Ocean and west Pacific (Figure 1) during the months of October through February from 1998 to 2011. The west Pacific Ocean is further separated into the three subregions—the northwest, northeast, and southeast—since the precipitating cloud population and large-scale environment markedly vary between these regions. These differences will be discussed in detail in the following sections. We have not included land areas in this analysis, so the southwest portion of the west Pacific Ocean is excluded. Every echo feature is described by its intensity using 3-D attenuation corrected reflectivity from the TRMM 2A-25 product [*Iguchi et al*., 2000a, 2000b] and separated into its echo rain type using the classification provided in the TRMM 2A-23 product [*Awaka et al*., 1997]. The analysis reported here was done before the version 7 data products were available. The results of this study would not change if version 7 products were used since our study is based primarily on reflectivity fields and simple level 2 products (convective, stratiform, and shallow isolated categorization), which were not significantly affected by the version update.

[13] With a sensitivity of 17 dBZ, the TRMM PR detects most of the rainfall in tropical oceanic regions and a considerable amount of the vertical structure of storms. Here we use the TRMM PR data to analyze four important components of the precipitating cloud population. The TRMM 2A-23 product divides the PR data into three categories: convective, stratiform, and other [*Awaka et al*., 1997]. These categories are first used to separate each contiguous 3-D radar echo into its convective and stratiform components. Four subsets of convective echoes are identified in order to capture fundamentally different characteristics of convective entities. One subset includes all isolated shallow precipitating convective elements of the type analyzed previously by *Schumacher and Houze* [2003]. We refer to these entities as isolated shallow echoes (ISEs), and they represent precipitating echoes whose echo tops are at least 1 km below the 0°C level. To capture more intense convection, we consider two features defined by an echo threshold of 30 dBZ. These entities are similar to those analyzed by *Houze et al*. [2007], *Romatschke et al*. [2010], and *Romatschke and Houze* [2010] to investigate extreme convective systems over land. However, the convective reflectivity thresholds used in this study are lowered from 40 to 30 dBZ to be consistent with differences between oceanic and land convection. We tried different thresholds, and while all were qualitatively consistent, the 30 dBZ threshold most clearly distinguishes qualitative differences in the echo populations. Deep convective cores (DCCs) are identified as contiguous 3-D convective columns with radar echo $\geq$30 dBZ reaching at least 8 km in altitude. DCCs represent young, vigorous convection that is sometimes contained within MCSs. Wide convective cores (WCCs) are defined as contiguous 3-D convective volumes with radar echo $\geq$30 dBZ covering at least 800 km^2 at some altitude. Given that WCCs identify the most horizontally expansive convective cores, these echo features are more commonly associated young MCSs. Thus, DCCs and WCCs are not mutually exclusive and are two different indications of convective intensity whose populations often overlap but do not coincide. A large region

of convectively initiated stratiform precipitation is a manifestation of a well-developed MCS [*Houze*, 1993, 2004]. To signify such a feature, a broad stratiform region (BSR) is defined as a contiguous stratiform echo covering at least 50,000 km^2. BSRs have no reflectivity threshold. In this study, we take a census of the four above-defined echo object types (ISE, DCC, WCC, and BSR) as a means of determining the nature and variability of the precipitating cloud population associated with the MJO.

[14] To relate the populations of these observed radar echo objects to the evolving large-scale environmental conditions associated with the MJO, we analyze the large-scale circulation patterns, relative humidity stratification, and vertical wind shear fields within which the clouds occur using four-times-daily ERA-interim reanalysis [*Dee et al*., 2011] at 1.5° × 1.5° degree resolution for the same geographic regions and time periods examined in the TRMM PR portion of this study. *Tian et al*. [2010] compare the moist vertical profile of the ERA-interim reanalysis and satellite data from the Atmospheric Infrared Sounder (AIRS) with respect to the MJO in the Indian and west Pacific Oceans. While discrepancies between the global reanalysis and satellite exist, including an underestimation of boundary layer moisture by the reanalysis, the ERA-interim reanalysis provides the most reasonable reanalysis representation of the large-scale humidity and circulation fields.

[15] We use the *Wheeler and Hendon* [2004] real-time multivariate MJO index (RMM index) to group the TRMM PR data and ERA-interim reanalysis in relation to the structure of the MJO. To ensure that composites represent robust MJO events, we consider only the months of October through February, which encompass the climatological peak of the MJO season [*Madden*, 1986]. We only include days in which the amplitude of the RMM index is greater than one to assure that we are representing well-defined MJO events. While *Roundy et al*. [2009] showed that the RMM index may be impacted by Kelvin wave activity and *Straub* [2012] indicated that the index may not always appropriately capture MJO initiation, these flaws likely have a minor impact on the results of the current study since we analyze long-term composites of observational data with an emphasis on well-developed MJO events in boreal winter.

[16] During the 14 boreal winters in the TRMM PR data set, approximately 63% of the days are characterized by a robust MJO. In order to determine if the precipitating cloud population significantly varies with phase of the MJO, a statistical technique called bootstrapping is used to create 20 realizations of the data in each phase. Each realization is created by sampling 100 days from a given phase with replacement which requires that each day is returned to the full data set before the next day is selected. Thus, each day in a realization is selected from the full, original data set, and an individual day may be repeated in any one realization of 100 days. This process enables each realization to be slightly different but still accurately capture the overall characteristics of the full data set. By averaging the means of each realization, we estimate the mean of the full, original data set. Then, we calculate the 99% confidence interval of the estimated mean using the 20 realizations and assess if precipitating cloud population significantly varies with phase of the MJO. The mean of the 20 realizations is almost identical to the mean of all the days in a given phase (not shown), which confirms that the realizations accurately represent the full data set and its variability. For this reason, the ERA-interim reanalysis composites are generated using all days for which we have analyzed radar data in a given phase. It is important to note that an individual MJO event may display stronger or more abrupt variability than the composites presented in the current study since this study analyzes composites based on phases of RMM index and the duration of each phase varies for individual MJO events. Evidence of this smoothing will be further discussed in section 7 with reference to the Dynamics of the Madden-Julian Oscillation (DYNAMO)/Atmospheric Radiation Measurement-MJO Investigation Experiment (ARM-AMIE) campaigns that took place from 1 October 2011 to 9 February 2012 in the central Indian Ocean.

3. Variations in the Precipitating Cloud Population With Phase and Region

[17] Figure 2, from *Wheeler and Hendon* [2004], shows how satellite-observed outgoing long-wave radiation (OLR) varies by phase of the MJO. The black vertical lines show the geographic regions analyzed in the current study. The active phase, indicated by a minimum of OLR, propagates eastward such that it is centered over the central Indian Ocean during phase 3 and over the west Pacific Ocean in phases 5–6. While the eastward propagation of the convective envelope of the MJO is readily apparent in OLR, the composition of the cloud population (by size and type of cloud) is not well discriminated. In this section, we use TRMM PR data to demonstrate how the composition of the precipitating cloud population varies from one phase to the next over the central Indian and west Pacific Oceans.

[18] Figures 3–6 show maps of the spatial distribution of the frequency of ISE, DCC, WCC, and BSR echoes, respectively, over the two areas of study. The data are averaged over the 20 realizations in the central Indian and west Pacific Oceans during phases 1, 3, 5, and 7. This frequency represents how often the TRMM PR detects one of these echo entities in a 0.5° × 0.5° grid box and is thus a measure of the areal coverage of each echo feature. Since this study focuses only on the oceanic precipitating cloud population, any grid box containing land is blank in the maps. The color bar differs in each figure to most clearly depict the variability of each echo feature. The black lines in the west Pacific maps show the boundaries of the northwestern, northeastern, and southeastern subregions.

[19] Figure 7 summarizes the variability of the echo features within the oceanic domains shown in Figure 1 (central Indian Ocean and northwestern, northeastern, and southeastern portions of the west Pacific Ocean) and plots the frequency by phase. The blue lines represent the 20 realizations, the black line is the mean of the realizations, and the dashed red lines represent the 99% confidence interval of the true mean based upon the 20 realizations. The active phase in each geographic region is defined in this study to occur during the phase that has the maximum areal coverage of BSR echoes. Thus, phases 2–3 constitute the active phase in the central Indian Ocean, phase 5 in the northwestern portion of the west Pacific, phases 3–7 in the northeastern portion of the west Pacific Ocean, and phase 6 in the southeast portion of the west Pacific Ocean. While comparison

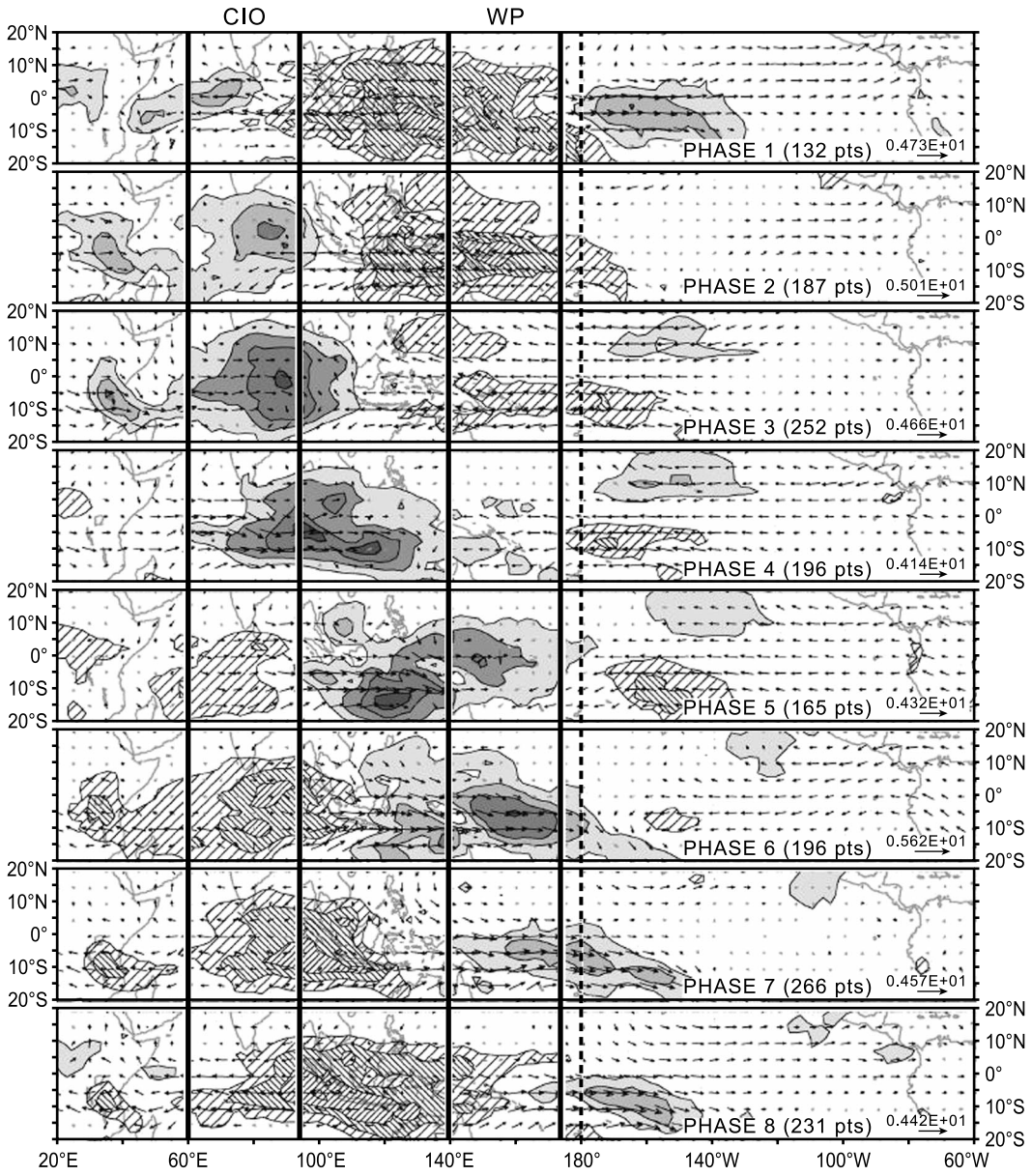


Figure 2. December, January, and February composite of OLR and 850 hPa wind anomalies during each phase of the MJO from 1979 to 2001 from *Wheeler and Hendon* [2004]. Negative OLR anomalies are shaded, positive OLR anomalies are hashed, and wind anomalies significant at the 99% confidence level are in black. The total number of days in each phase and magnitude of the largest wind anomaly are in the lower right of each panel.

of Figures 3–6 reveal that BSR echoes in the central Indian and west Pacific Oceans experience the greatest variability in areal coverage with phase of the MJO, Figure 7 shows that the areal coverage of each echo entity significantly varies with phase in all geographic regions.

[20] ISEs are shown in Figure 3 to always be present in each geographic region. These echoes are especially common along a horizontal band near 8°S in the central Indian Ocean and 8°N in the west Pacific Ocean. *Schumacher and Houze* [2003] showed that these bands of enhanced ISE frequency are associated with the poleward edges of the Intertropical Convergence Zone (ITCZ), which is climatologically located in the southern hemisphere in the central Indian Ocean and on both sides of the equator in the west Pacific Ocean. Inspection of Figure 3 reveals that ISEs are slightly less common during the active stage of the MJO, which occurs during phase 3 in the central Indian Ocean and phase 5 in the west Pacific Ocean. Despite the visually subtle variability, Figures 7a, 7e, 7i, and 7m indicate that ISEs are significantly more frequent during the suppressed stage than the active stage in each geographic region. Figures 3 and 7 normalize the ISE coverage by the total area detected by the TRMM PR, which includes echo-covered and echo-free areas. If ISE coverage is normalized only by the echo-free area, ISE coverage continues to vary with phase and notably peak during the suppressed stage of the MJO (not shown), from which we conclude that the variability of ISE coverage with phase of the MJO is not purely attributable to ISEs having less space to develop when deep and wide convective activity greatly increases during the active stage. Figure 3 indicates that the greatest reduction of

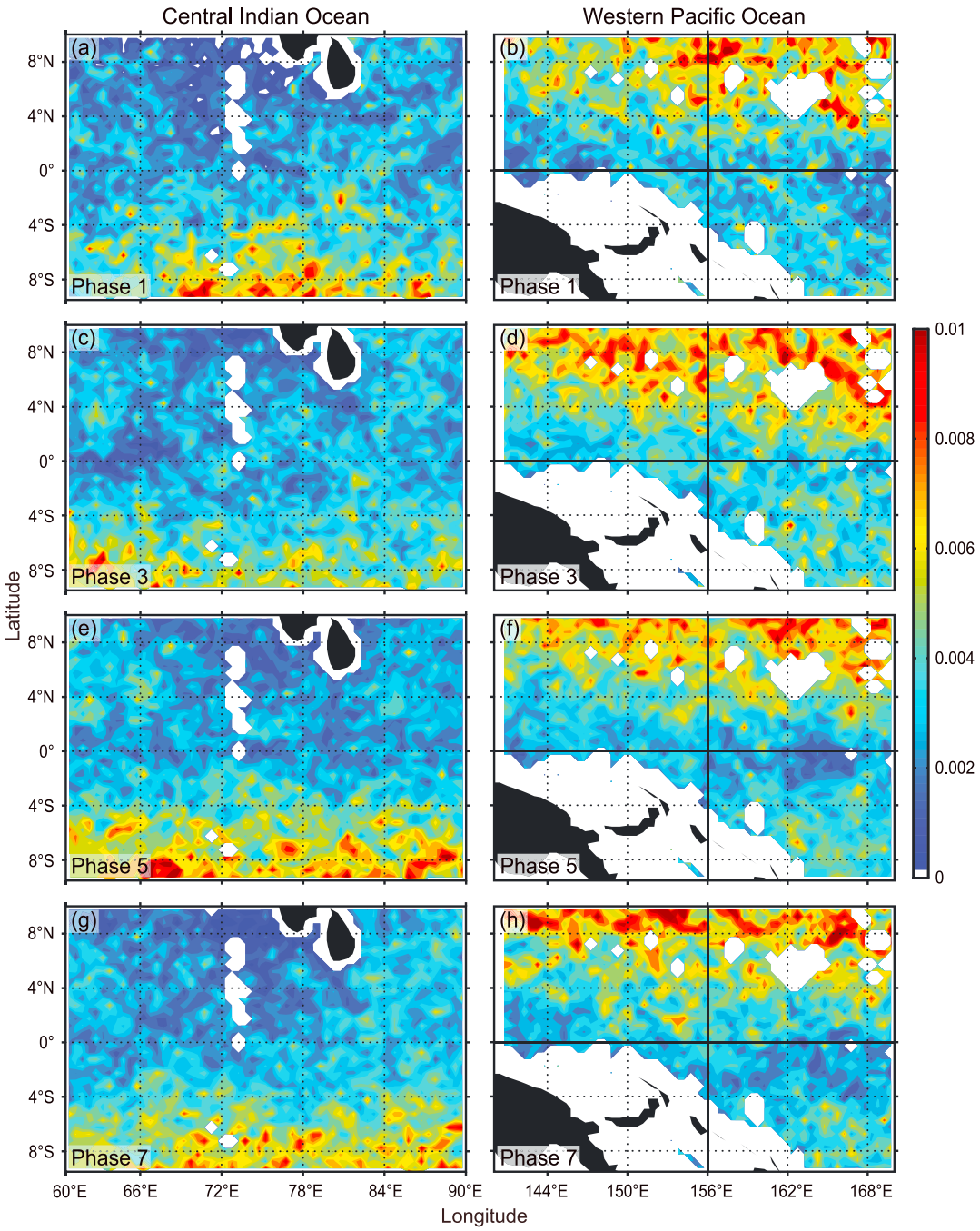


Figure 3. Geographic distribution of ISE frequency over the central Indian and west Pacific Oceans during phases 1, 3, 5, and 7 averaged over the 20 realizations in each phase. The frequency is defined as the number of TRMM PR pixels in a 0.5° × 0.5° grid box that contain an ISE normalized by the total number of TRMM PR pixels detected in that grid box, which includes both echo-covered and echo-free pixels. Any grid box containing land is excluded and left blank. The resolution of a TRMM PR pixel is 0.05° × 0.05°. The black lines in the west Pacific Ocean show the boundaries of the northwestern, northeastern, and southeastern subregions.

ISEs in the central Indian Ocean occurs within the ITCZ region near 8°S, which suggests that the suppressed stage of the MJO in the central Indian Ocean coincides temporally with the active stage of the ITCZ in the central Indian Ocean. While both regions experience a maximum in ISE coverage during the suppressed stage, the ISE maximum in each geographic region occurs in different phases of the suppressed stage. Figure 7a shows that ISE occurrence peaks in the central Indian Ocean in phase 5, which is two phases after the active stage and during the beginning of suppressed stage. However, ISEs in the west Pacific Ocean are shown in Figures 7e, 7i, and 7m to peak in phase 3, which is five to six phases after the active stage and during the end of the suppressed stage.

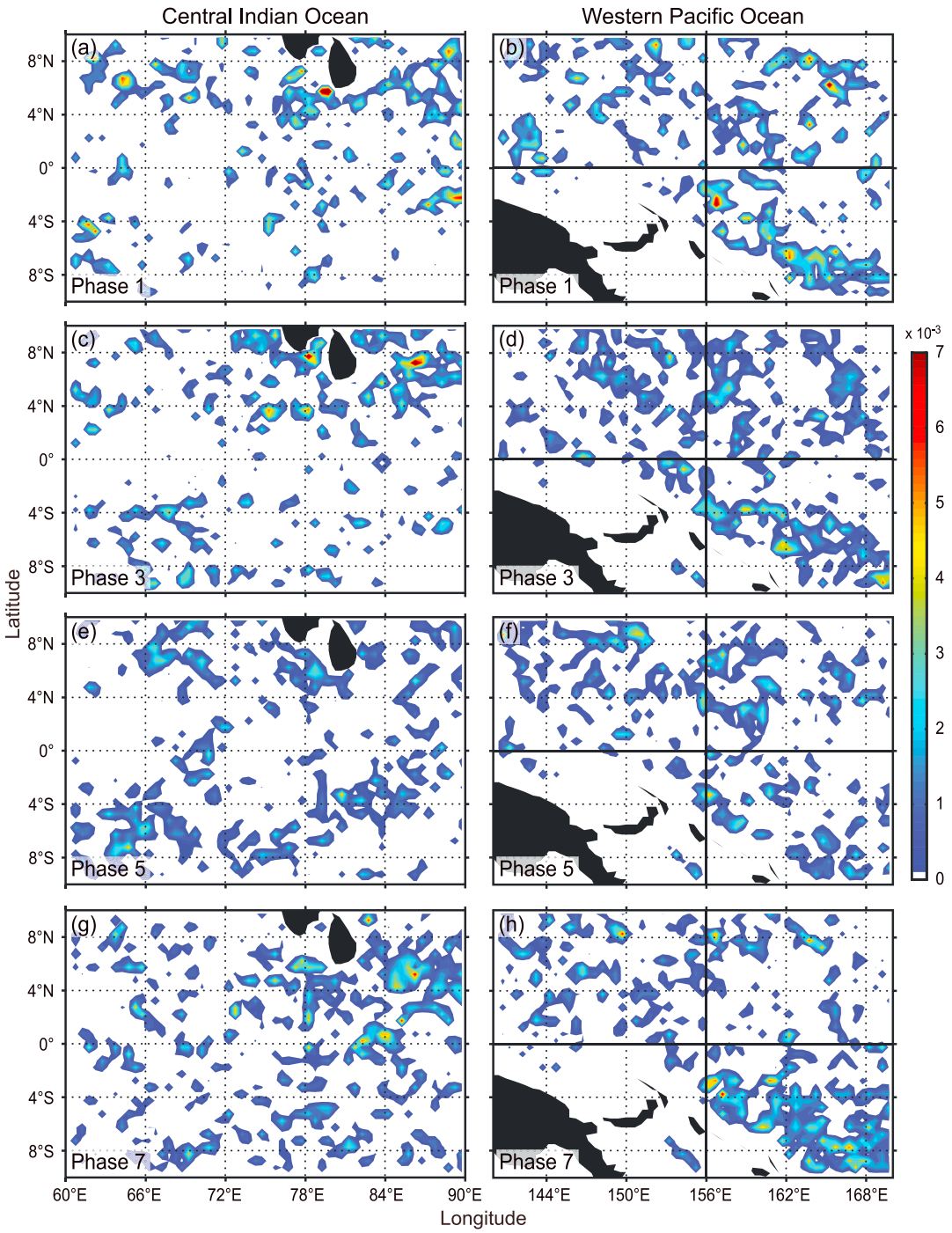


Figure 4. Same as Figure 3 except for DCCs.

[21] DCC echoes occur much less frequent than ISEs. However, like ISEs, DCC echoes are ever present, and their variability is not easily seen at first glance in Figure 4 but is shown to be statistically significant in Figure 7. Close examination of Figure 4, however, confirms that DCC echoes in the central Indian Ocean occur somewhat more frequently north and south of the equator. Figure 7b indicates that DCC echoes in the central Indian Ocean broadly peak during the active stage of the MJO in phases 1–3. However, this peak is not significantly greater than another peak occurring just prior to the active stage in phase 7. Comparison of the panels in Figure 4 indicates that DCC echoes are overall more common in the west Pacific Ocean than the central Indian Ocean. The consistently warmer sea surface temperatures (not shown) and higher instability in the west Pacific Ocean might account for the DCC being more common in the west Pacific. The DCC echoes are inhomogeneously spread across the west Pacific Ocean, with these echoes being somewhat more common over the warm pool and the South Pacific Convergence Zone (SPCZ), which are contained with the northwestern and southeastern portions of the west Pacific Ocean, respectively. The annual mean

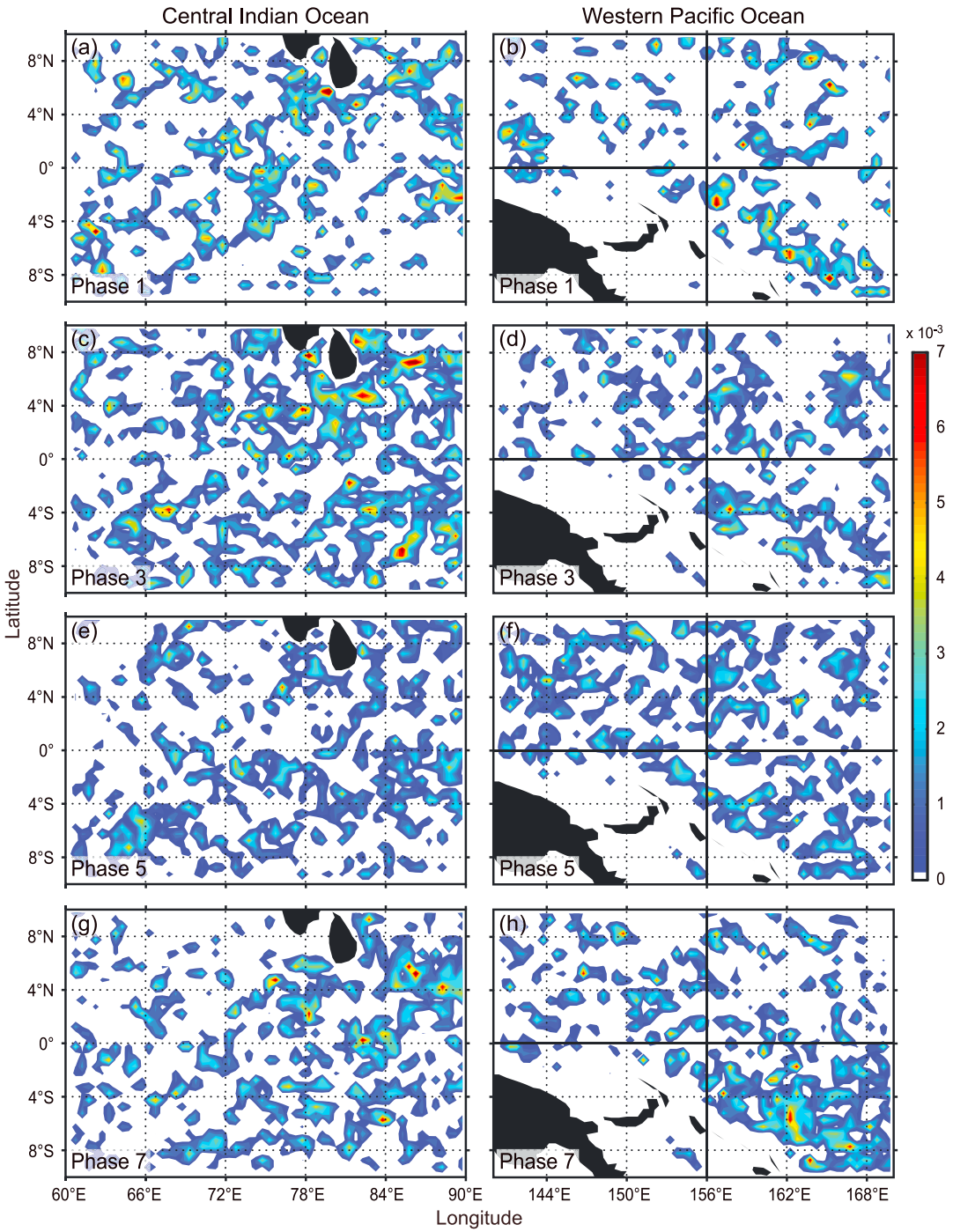


Figure 5. Same as Figure 3 except for WCCs.

position of the SPCZ is along a diagonal from 10°S, 110°E to 30°S, 120°W [*Vincent*, 1994]. While Figures 7f and 7j indicate that DCC echoes in northwestern and northeastern portions of the west Pacific Ocean do not experience a statistically significant peak, Figure 7n shows that the occurrence of DCC echoes in the southeastern portion of the west Pacific Ocean peaks distinctly at the end of the active stage in phase 7. The absence of a peak in frequency of DCC echoes during the active stage in the northeastern portion of the west Pacific may be related to the tendency for the convection associated with the MJO to leave the equatorial belt in the west Pacific Ocean and manifest most clearly in the region of the SPCZ where the water is warmer [*Weickmann et al.*, 1985].

[22] WCC echo variability with phase of the MJO in the central Indian and west Pacific Oceans is more visually identifiable in Figure 5 than the ISE and DCC echo variability in Figures 3 and 4, respectively. In the central Indian Ocean, WCC echoes are homogeneously distributed as they peak during the active stage in phase 3, which Figure 7c indicates is statistically significant. Furthermore, Figure 7c indicates that the increase in WCC echo occurrence leading up to

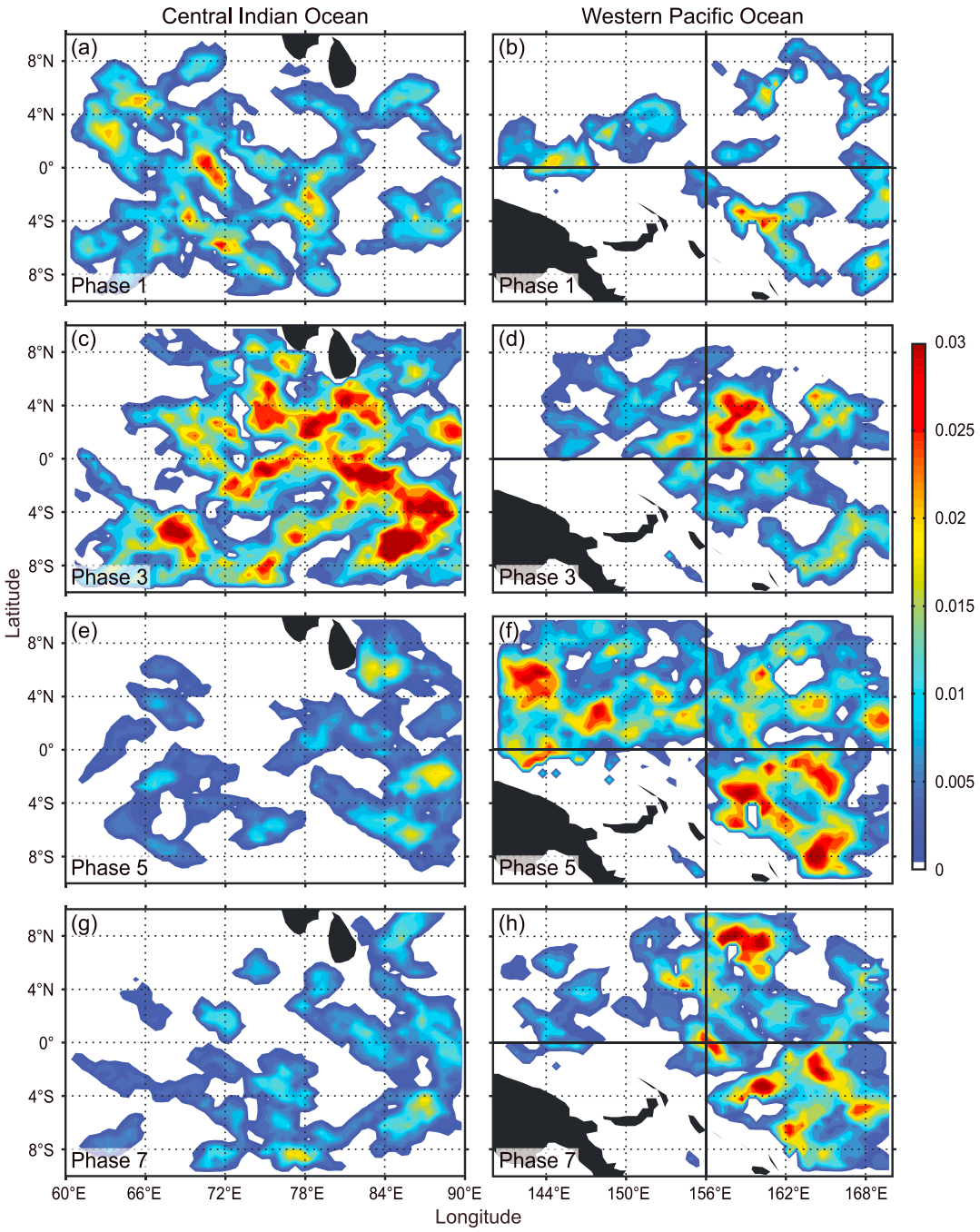


Figure 6. Same as Figure 3 except for BSRs.

the active stage in the central Indian Ocean is more gradual than the reduction immediately following the active stage. A minimum in occurrence is also evident in Figure 7c during phase 5; however, this minimum could be considered to extend broadly across phases 4–8. Comparing the panels of Figure 5 suggests that WCC echoes occur more frequently in the central Indian Ocean than in the west Pacific Ocean. WCC echoes in the west Pacific Ocean are shown in Figure 5 to continue to preferentially occur along a diagonal from the warm pool in the northwestern portion of the west Pacific Ocean to the SPCZ in the southeastern portion of the west Pacific Ocean. Figure 7o indicates that the southeastern portion of the west Pacific Ocean experiences a significant maximum in WCC echo coverage during phase 7, one phase after the active phased defined by the maximum occurrence of BSR echoes. The increase and decrease in WCC coverage in the southeastern portion of the west Pacific Ocean are more symmetric with respect to phase than in the central Indian Ocean (Figure 7c). WCC echoes broadly minimize in the southeastern portion of the west Pacific Ocean during phases 2–5. The peak frequency of WCC echoes in the northwestern portion of the west Pacific Ocean is shown in Figure 7g to be less distinct, as the frequency increases stepwise starting in phase 2 and maximizes during phase 6, which is also one phase after the BSR maximum and active phase. However, the maximum in phase 6 is not statistically

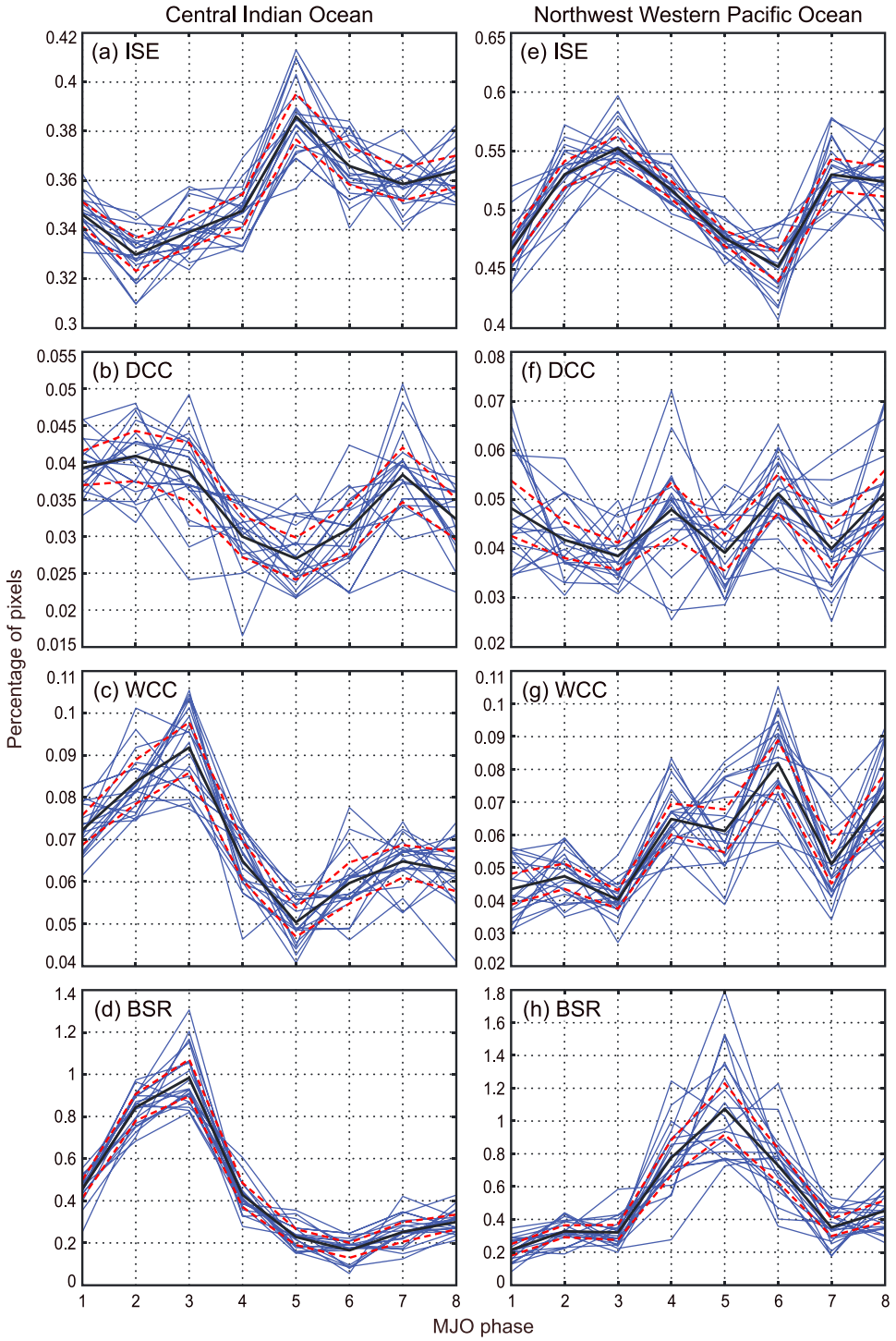


Figure 7. (a) Total ISE frequency in the central Indian Ocean. The frequency is defined as the number of TRMM PR pixels in the central Indian Ocean that contain an ISE normalized by the total number of TRMM PR pixels detected in the central Indian Ocean, which includes both echo-covered and echo-free pixels. The frequency is reported as a percent. The blue lines show the frequency-phase series for the 20 realizations, the black line is the mean of the realizations, and the dashed red lines are 99% confidence interval of the mean and are calculated using the Student's *t* statistic. (b) Same as Figure 7a except for DCCs in the central Indian Ocean. (c) Same as Figure 7a except for WCCs in the central Indian Ocean. (d) Same as Figure 7a except for BSRs in the central Indian Ocean. (e–h) Same as Figures 7a and 7b except in the northwestern portion of the west Pacific Ocean. (i–l) Same as Figures 7a and 7b except in the northeastern portion of the west Pacific Ocean. (m–p) Same as Figures 7a and 7b except in the southeastern portion of the west Pacific Ocean.

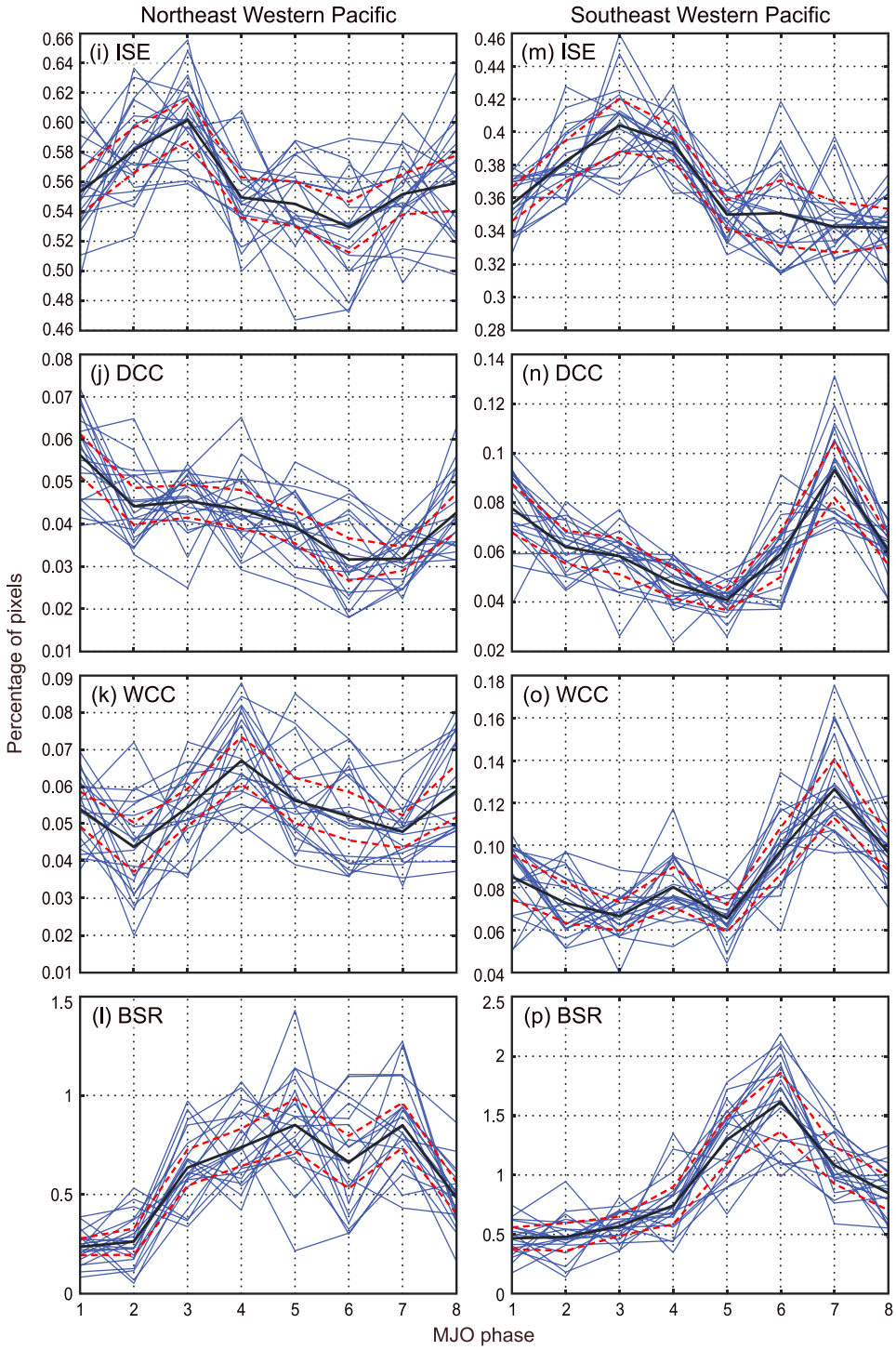


Figure 7b. (continued)

larger than a secondary peak during phase 8. WCC variability in the northeastern portion of the west Pacific Ocean is distinctly different. While a single peak in WCC echo coverage occurs during the active stage of the MJO in the northwestern and southeastern portions of the west Pacific Ocean, Figure 7k shows that WCC echoes in the northeastern portion of the west Pacific Ocean maximize and minimize in coverage twice. After minimizing in phase 2 and maximizing in phase 4, WCC echoes in the northeastern portion of the west Pacific Ocean gradually decline to a secondary minimum in phase 7 and increase to a secondary maximum in phase 8. These latter minima or maxima are not statistically distinct. This departure in the behavior of WCC echoes in these regions may be related to the tendency for the MJO to avoid the Pacific cold tongue and propagate into the SPCZ [*Weickmann et al.*, 1985].

[23] BSR echoes display the most visually apparent variability with phase of the MJO as they maximize in the active

stage and minimize during the suppressed stage in each region (Figure 6). This trend could be expected since BSR echoes are the most laterally extensive of the echo entities used in the current study to represent the precipitating cloud population, and their maximum designates the phases hosting the most frequent upscale growth of deep convection into organized MCSs. Satellite OLR analysis has also shown MCSs to exhibit the greatest variability of all convective entities over the warm tropical Pacific and Indian Oceans [e.g., *Chen et al*., 1996]. Figure 7 indicates that the variability of the precipitating cloud population during the MJO is best characterized by a reduction in large, mesoscale systems during a relatively long suppressed stage. In the central Indian Ocean, BSR echoes maximize during phases 2–3, which Figure 7d shows is highly significant. Additionally, Figure 7d indicates that the variability in BSR echo coverage is asymmetric around the active stage as BSR echo coverage increases slowly leading up to the active but decreases rapidly after the active stage. The eastward propagation of the MJO is discernible in Figure 6. In the central Indian Ocean, BSR echoes tend to occur in the western portion the region during phases 8–1 and in the central and eastern portions during phases 2–7. Over the west Pacific Ocean, BSR echoes continue to preferentially propagate gradually eastward. Figures 7h, 7l, and 7p emphasize, however, an inherent spatial variability of BSR occurrence in the west Pacific Ocean. While the northwestern and southeastern portions have statistically significant BSR maxima during phases 5 and 6, respectively, the northeastern portion has a broad peak during phases 3–7. Additionally, BSR echoes in the southeastern portion vary asymmetrically around the active phase similar to the central Indian Ocean, but BSR echoes in the northwestern portion vary symmetrically.

[24] In summary, Figure 7 shows that within each region (central Indian and west Pacific Oceans), the composition of the precipitating cloud population changes in terms of the different sizes and types of precipitating clouds present as the MJO transitions from one phase to the next. Additionally, Figure 7 illustrates that the relationship between the population and MJO phase changes between the time that the MJO occurs in the central Indian Ocean and propagates into the west Pacific Ocean. Generally, the frequency of large stratiform regions decreases drastically during the suppressed stage of the MJO in both geographic regions. In the central Indian Ocean, ISEs are most common just after the active stage, and the peaks in occurrence of DCC, WCC, and BSR echoes maximize synchronously, which suggests that the active stage is characterized by deep convection of all sizes and stages of development. In the west Pacific Ocean, ISEs maximize just prior to the active stage and DCC, WCC, and BSR echoes do not simultaneously maximize. With the exception of the northeastern portion, WCC echoes in the west Pacific Ocean maximize one phase after BSR echoes peak, which suggests that throughout most of the west Pacific Ocean, the active stage is first characterized by extremely large MCSs followed by smaller MCSs. The northeastern portion of the west Pacific Ocean has the least coherent variability with phase of the MJO, which may be associated with the tendency for the convective envelope of the MJO to manifest more strongly off the equator over the warmer water of the SPCZ region.

[25] Figure 8 compares the magnitude of the overall variability of each type of echo object (ISE, DCC, WCC, and BSR). Figures 8a–8d show the mean frequency (thick line) and 99% confidence interval (thin lines) of ISEs, DCCs, WCCs, and BSRs in terms of areal coverage. From these panels, we see that BSR echoes dominate the variability in areal coverage of the precipitating cloud population in each geographic region and occur primarily in the active stage of the MJO. However, areal coverage is just one way of characterizing the variability of the precipitating cloud population; it emphasizes occurrence in a way that determines when the upper-level heating, characteristic of the stratiform components of the convective population [*Houze*, 1982, 1989], is likely to be most prominent. The variability in the number of echo entities is another important aspect of the precipitating cloud population, which emphasizes the occurrence of convective-scale elements most responsible for lower-level mass transport and convective heating. Figures 8e–8h show the mean (thick line) and 99% confidence interval (thin line) of the number of DCCs, WCCs, and BSRs as a function of phase of the MJO. Figures 8i–8l show the mean and 99% confidence interval for the number of ISEs. ISEs are by far the most common and variable element of the precipitating cloud population by number in all geographic regions. The deep convective heating profile maximizing in mid-levels is represented by the intense convective DCC and WCC echo categories. WCC echoes are most common and experience the greatest numerical variability in the central Indian Ocean. In the west Pacific Ocean, however, DCC echoes are most common in terms of number. While ISE, DCC, and WCC echoes experience only subtle changes in areal coverage, these echo entities are highly variable in terms of their number.

4. Concurrent Relationships Between Relative Humidity and the Precipitating Cloud Population

[26] *Haertel et al*. [2008] showed that the large-scale circulation of the MJO is sensitive to the particular mixture of heating by shallow convection, deep convection, and stratiform elements of MCSs present in a given phase. The mix of echo types that we have considered in the previous section shows how the cloud population in each phase of the MJO is a distinctly different combination of convective element types. Understanding the relationship of these heating element combinations to the large-scale circulation is a major goal of MJO research. To begin to address this objective, we investigate in the remainder of this paper how the large-scale circulation varies in concert with the convective population indicated by the TRMM PR data. In this study, we cannot determine whether the large-scale midtropospheric relative humidity is a reaction to or caused by changes in the precipitating cloud population. Nevertheless, we can learn a great deal from examining the changes in large-scale conditions that are concurrent with the changes in the makeup of the cloud population from one phase of the MJO to the next that we examined in section 3. Any numerical model employed to investigate the cause and effect relationships between cloud population and large-scale environment will have to be consistent with the data examined here.

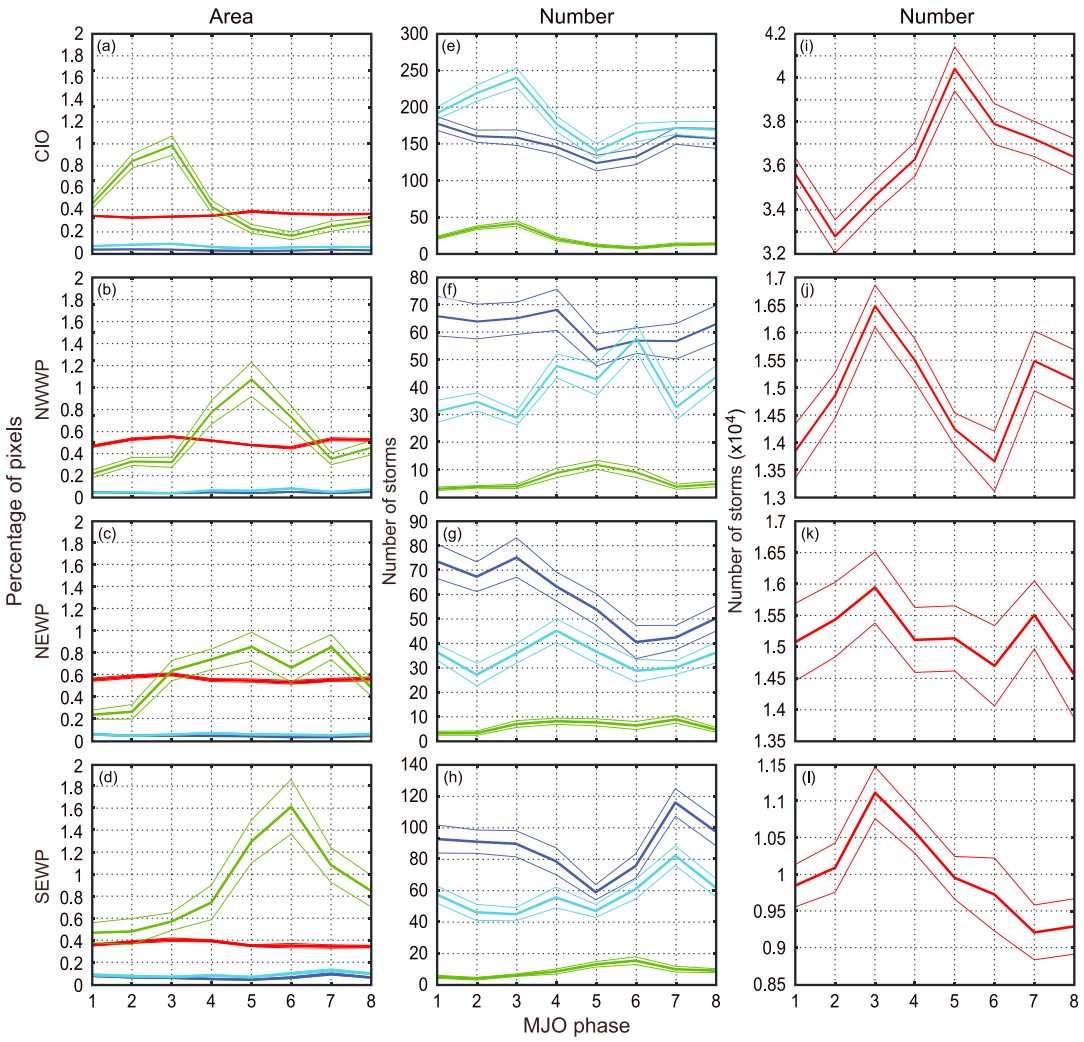


Figure 8. (a–d) The average total frequency (thick line) and 99% confidence interval of the 20 realizations for ISEs (red), DCCs (dark blue), WCCs (cyan), or BSRs (green) in the central Indian Ocean and northwestern, northeastern, and southeastern portions of the west Pacific Ocean. The frequency is defined as the number of TRMM PR pixels in the central Indian Ocean that contain an ISE normalized by the total number of TRMM PR pixels detected in the central Indian Ocean, which includes both echo-covered and echo-free pixels. (e–h) The average number (thick line) and 99% confidence interval (thin line) of the 20 realizations for DCCs (dark blue), WCCs (cyan), and BSRs (green) in the central Indian Ocean and northwestern, northeastern, and southeastern portions of the west Pacific Ocean. (i–l) The average number (thick line) and 99% confidence interval of the 20 realizations for ISEs in the central Indian Ocean and northwestern, northeastern, and southeastern portions of the west Pacific Ocean.

[27] To begin this exploration, Figure 9 shows the vertical profile of relative humidity, averaged over all oceanic grid points in each geographic region from the ERA-interim reanalysis. The ERA-interim fields used in this and all subsequent figures are composited from the exact days on which the TRMM PR echoes analyzed in the previous figures were taken. In each panel, the solid lines represent the convectively active phase with the solid black and blue lines representing the two phases leading up to the active stage. The solid green line represents the convectively active stage corresponding to the peak occurrence of BSR echoes, and the solid red line represents the phase immediately following the active phase. The dashed lines represent the suppressed phases. Regardless of phase and geographic region, the average large-scale relative humidity in Figure 9 is consistently moist below 800 hPa, i.e., the large-scale near-surface moist layer never goes away! This uniformity is consistent with previous studies [e.g., *Lin and Johnson*, 1996; *Powell and Houze*, 2013] and indicates that variations in the precipitating cloud population analyzed in section 3 are not associated with the large-scale lower-tropospheric (1000–800 hPa) relative humidity field.

[28] The greatest large-scale moisture variations in both geographic regions are found in the mid-upper troposphere from 700 to 200 hPa and are characterized by a relative humidity maximum during the active stage and minimum during the suppressed stage. Figure 9 indicates that the greatest large-scale mid-tropospheric relative humidity variability occurs over the central Indian Ocean. The mid-tropospheric relative humidity in the central Indian Ocean rapidly increases from phase 7 to 8, just after the secondary

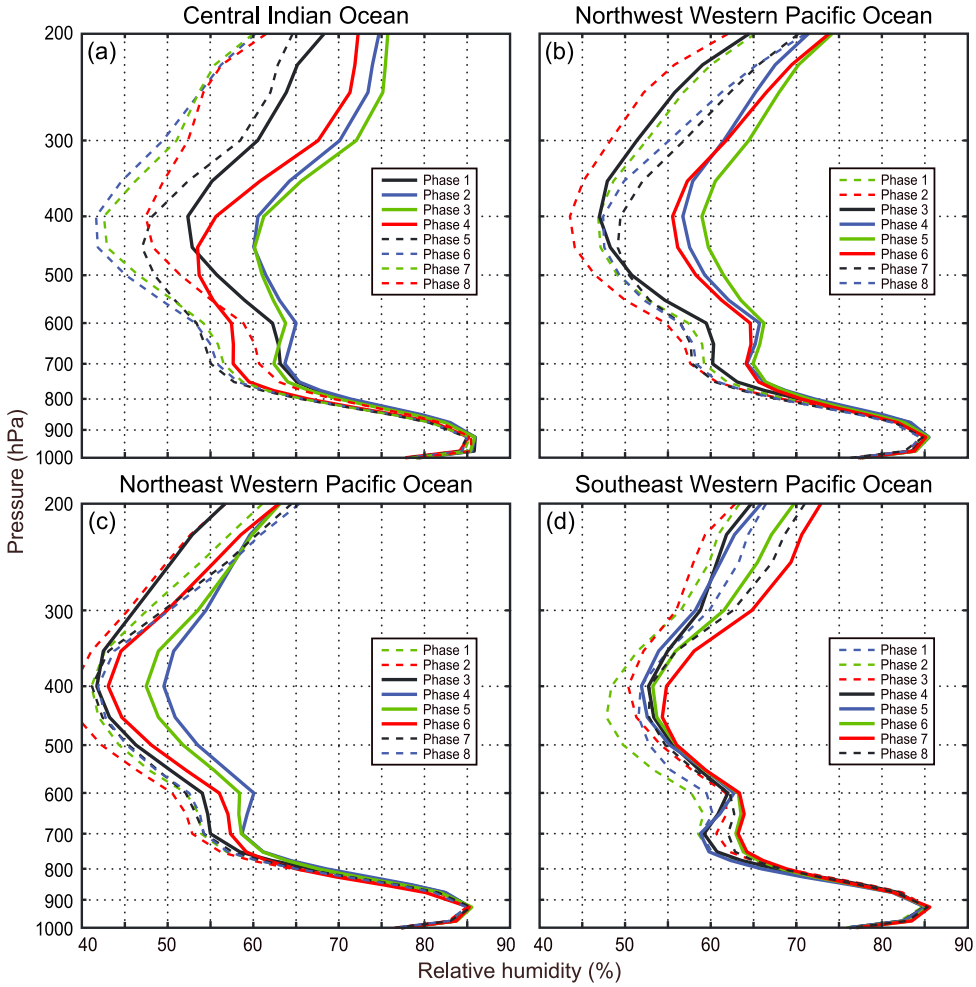


Figure 9. The average relative humidity profile for all oceanic grid points in the ERA-interim reanalysis in the central Indian Ocean and northwestern, northeastern, and southeastern portions of the west Pacific Ocean. Dashed lines represent the convectively suppressed phases in each region. Solid lines depict the convectively active phases, with the solid green line representing the phase with the largest areal coverage of BSRs in each region. The relative humidity is given as a percent.

peak in DCC echoes and just prior to significant increases in WCC and BSR echo coverage (Figures 7b–7d). Significant moistening prior to the onset of deep convection is consistent with previous observations [e.g., *Lin and Johnson*, 1996; *Kiladis et al*., 2005]. The source of moisture for this rapid increase in relative humidity is unclear but has been suggested to result from planetary wave induced vertical motion [e.g., *Hendon and Salby*, 1994], horizontal advection [e.g., *Tromeur and Rossow*, 2010], and/or accumulation from convective bursts occurring at shorter time scales [e.g., *Benedict and Randall*, 2007]. Mid-tropospheric relative humidity continues to increase slowly and maximize in phases 2–3, during which the areal coverage of DCC, WCC, and BSR echoes rapidly increases and maximizes (Figure 7b–7d). Finally, mid-tropospheric relative humidity quickly declines as the frequencies of DCC, WCC, and BSR echoes significantly decrease in phase 4. It is unknown if the mid-tropospheric moisture variability observed during the convectively active stage of the MJO is primarily the result of the eastward progression of the large-scale MJO circulation or is a product of the cloud population itself.

[29] Figure 9 indicates that the shape and variability of the relative humidity profile in the northwestern and northeastern portions of the west Pacific Ocean are similar to those in the central Indian Ocean. However, the profile in the southeastern portion of the west Pacific Ocean is notably different since variability in the 500–600 hPa layer is relatively small. Despite this reduced variability in the southeastern portion, each of the west Pacific Ocean regions displays a systematic association between the precipitating cloud population and mid-tropospheric moisture. For example, mid-tropospheric moisture in the northwestern portion of the west Pacific Ocean is shown in Figure 9 to maximize in phase 5, which corresponds to the maximum in BSR echo coverage in Figure 7h. Even though Figure 7h shows that BSR echoes significantly decline in phase 6, Figure 9 indicates that mid-tropospheric relative humidity does not greatly decrease until phase 7 when WCC echoes are shown in Figure 7g to significantly decline. The WCC peak and mid-tropospheric drying in the northwestern portion of the west Pacific Ocean is delayed by one phase relative to the central Indian Ocean, where the mid-troposphere dries

sharply one phase after DCC, WCC, and BSR echoes synchronously maximize. A similar trend is observed for WCC and DCC echoes in the southeastern portion of the west Pacific Ocean. Figure 9 shows that mid-troposphere (800–600 hPa) relative humidity begins to decline in the southeastern portion in phase 8, which is shown in Figures 7n–7p to be two phases after BSRs peak and one phase after DCC and WCC echoes peak. While it is unclear why the mid-troposphere dries one phase later in the west Pacific Ocean than the central Indian Ocean, we suggest that these persistent moist mid-tropospheric conditions in the west Pacific Ocean may be related to WCCs peaking one phase after BSRs peak in the west Pacific Ocean.

[30] Figures 7a and 8c indicate that ISEs are most common in the central Indian Ocean in phase 5, when the mid-troposphere is shown to be relatively dry in Figure 9. Figures 7e, 7i, 7m, and 9 indicate that ISEs in the west Pacific Ocean also peak out phase with the mid-tropospheric relative humidity peak. While these dry conditions may inhibit deep convection, shallow convection might be able to develop below this layer since the lower troposphere is always moist.

5. Concurrent Relationship Between Large-Scale Winds and the Precipitating Cloud Population

[31] Figure 10 shows maps of the 1000 hPa wind direction (vectors) and zonal speed (shading) average over all days for which we have analyzed radar data during phases 2, 4, 6, and 8 in the central Indian and west Pacific Oceans. The westerly wind burst (WWB) [*Zhang*, 2005] in the central Indian Ocean propagates eastward just south of the equator and maximizes during phase 4, which Figures 7b–7d indicate is one phase after DCC, WCC, and BSR echoes maximize. In general, the 1000 hPa winds near the equator in the central Indian Ocean remain westerly during each phase. While the WWB is observed in the west Pacific Ocean, the westerly winds are much weaker and more confined in the meridional direction. Additionally, the large-scale 1000 hPa winds in the northwestern and southeastern portions of the west Pacific Ocean switches from easterly during the suppressed stage to westerly during and following the active stage of the MJO. The WWB in the west Pacific Ocean propagates southeastward along the SPCZ in the southeastern portion of the west Pacific Ocean. Figure 10 indicates that the WWB peaks in the northwestern portion of the west Pacific Ocean during phase 6, one phase after BSR echoes maximize (Figure 7h), similar to the central Indian Ocean. However, unlike in the central Indian Ocean, WCC echoes maximize (Figure 7g) along with the WWB peak in phase 6. The southeastern portion of the west Pacific Ocean is also characterized by the peak WWB lagging the BSR maximum by one phase but occurring with the DCC and WCC maximum. Figure 10 indicates that low-level westerly winds minimize during phase 8 in the central Indian Ocean, which is near the minimum in BSR coverage and the end of the suppressed stage in Figure 7a. A similar association is observed during phase 3 throughout the west Pacific Ocean.

[32] Enhanced low-level westerlies following the convective maximum of the MJO has been previously documented [e.g., *Chen et al*., 1996; *Lin et al*., 2004], and a number of theories concerning the dynamical cause of these winds have been proposed. While the strong westerlies are clearly a characteristic of the Rossby wave component of the MJO [*Gill*, 1980; *Kiladis et al*., 2005], studies have also suggested that these westerlies may have a contribution from convective momentum transport by the MJO cloud population [e.g., *Moncrieff and Klinker*, 1997; *Houze et al*., 2000; *Mechem et al*., 2006; *Miyakawa et al*., 2012]. While the current study cannot deduce the dynamical cause of the enhanced westerlies, we suggest that the composition of the precipitating cloud population in a given phase is related to the observed large-scale low-level circulation field at that time. For example, the peak WWB may signal the conclusion of large, organized convection, as suggested by *Lau et al*. [1989].

[33] Figure 11 shows maps of the 500 hPa wind direction (vectors) and zonal speed (shading) in the central Indian and west Pacific Ocean regions, averaged over all days for which we have analyzed radar data in phases 2, 4, 6, and 8. In the central Indian Ocean, the WWB is readily apparent at 500 hPa, though weaker than at lower levels. While the 1000 hPa winds along the equator in Figure 10 are predominately westerly during each phase, the near equatorial winds at 500 hPa switch from easterly during the suppressed stages (Figures 11f and 11g) to westerly during and just following the active stage (Figures 11a and 11c). The 500 hPa westerlies maximize during phases 4–5 (Figure 11c), which Figure 7b–7d indicate is one and two phases after the DCC, WCC, and BSR peaks. The slightly longer lag between the convective maximum and peak 500 hPa WWB compared to the 1000 hPa WWB is consistent with the westward tilt of the MJO [*Sperber*, 2003; *Kiladis et al*., 2005]. Evidence of the WWB is also observed in the 500 hPa winds in the west Pacific Ocean, especially near the SPCZ in the southeastern portion during phases 7–8 (Figure 11h). However, the westerlies are weak, especially compared to the central Indian Ocean, and the westward tilt of the MJO is less apparent. The westerlies in the southeastern portion of the west Pacific Ocean peak in phase 7, which is shown in Figures 7n–7p to be one phase after the BSR maximum and during the DCC and WCC peaks.

[34] Figure 12 shows maps of the 200 hPa wind direction (vectors) and zonal speed (shading) in the central Indian and west Pacific Ocean regions, averaged over all days for which we have analyzed radar data during phases 2, 4, 6 and 8. Strong easterlies dominate the upper levels in the central Indian Ocean during the active phase of the MJO (Figure 12a). These easterlies propagate eastward along the equator and maximize in phase 4, which is shown in Figures 7b–7d to be one phase after the DCC, WCC, and BSR maxima. Figure 12 indicates that the circulation field in the central Indian Ocean has a sizable meridional component during phases 6–8, which corresponds to the suppressed stage of the MJO in that region. While Figure 12 shows that easterlies are also common in the west Pacific Ocean during active stage and propagate eastward, the easterlies are much weaker than the central Indian Ocean. Figure 12 shows that the areal coverage of strong easterly winds in the northeastern portion of the west Pacific Ocean maximizes in phase 8 which is one phase after the broad peak in BSRs (Figure 7l). While upper-level easterly winds in the northwestern portion of the west Pacific Ocean also maximize in terms of areal coverage during phase 8, Figure 7f

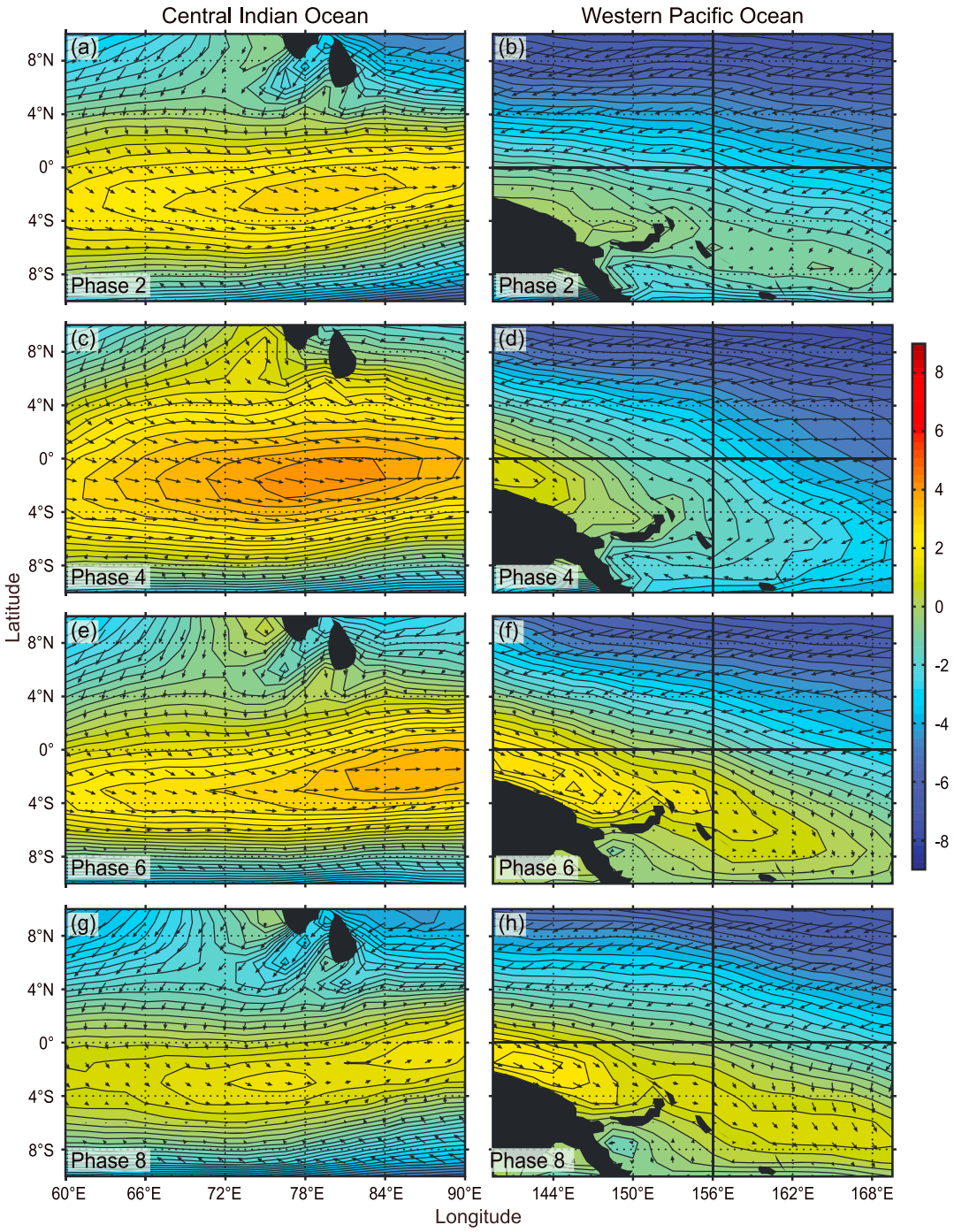


Figure 10. The average direction (vectors) and zonal speed (shading) of the 1000 hPa wind in the central Indian and west Pacific Oceans for all days during phases 2, 4, 6, and 8 in m s^{-1}. The black lines in the west Pacific Ocean show the boundaries of the northwestern, northeastern, and southeastern subregions.

shows that this easterly maximum is two phases after BSRs peak in that region. This two-phase lag in the maximum coverage of easterly 200 hPa winds with respect to the BSR maximum is also observed in the southeastern portion of the west Pacific Ocean. While the lag between the 200 hPa easterly maximum and BSR peak varies between one and two phases in the west Pacific regions, upper-level easterly winds consistently maximize shortly after the deepest and widest mesoscale echo entities peak.

6. Concurrent Relationship Between Large-Scale Shear and the Precipitating Cloud Population

[35] While thermodynamic and moisture stratification determine whether convection can or cannot exist, and how high into the atmosphere the clouds can penetrate, wind shear also influences convection. The environmental shear affects the in-cloud vorticity through tilting and stretching by the convective motions, and it affects the ability of the

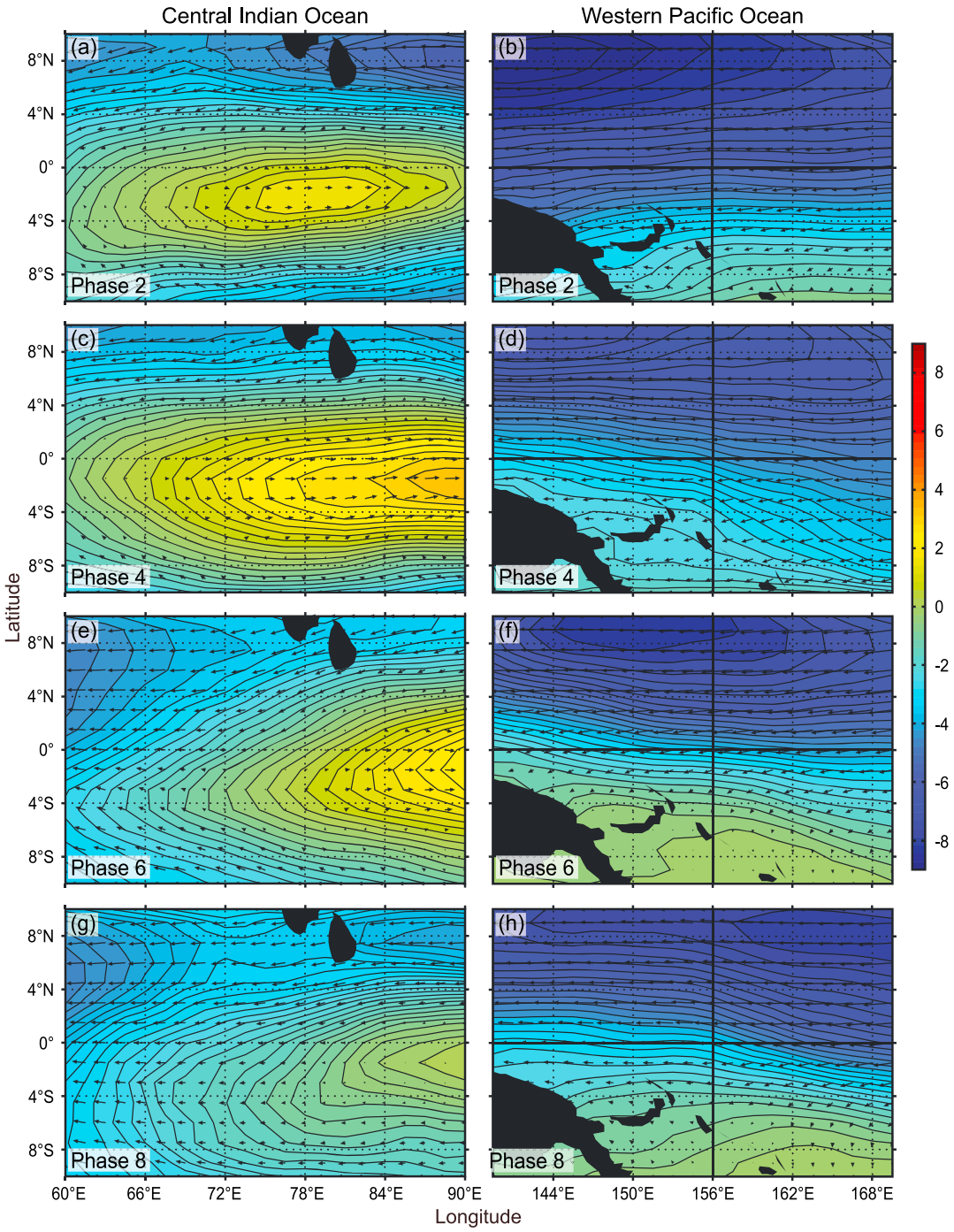


Figure 11. Same as Figure 10 except for the average 500 hPa wind.

convection to form mesoscale systems with attached stratiform regions (for details, see *Houze* [1993], chapters 8–9; *Houze* [2004]; and others). Since the wind fields of the different phases of the MJO, shown in the previous section, are characterized by strong differences between the winds at low, middle, and upper levels, we expect the shear patterns to be related to the nature of the convective population in any given phase of the MJO.

[36] Figure 13 employs the same color scheme as Figure 9 to show the vertical profile of zonal winds, averaged over all oceanic grid points in each geographic region. The solid red line, which represents the profile of zonal winds one phase after BSR echoes peak, is characterized by a maximum in westerly winds (or minimum in easterly winds) at approximately 750 hPa in each region. The maximum occurring just after the active phase is consistent with the behavior of the WWB noted in this phase in Figures 10 and 11. Figure 13 also indicates that zonal winds differ above 500 hPa in the central Indian and west Pacific Oceans. Not only does the shape of the profiles differ within the 500–200 hPa layer, but the high-level easterlies become much stronger in the central Indian Ocean and the maximum upper-level easterlies occur during the active stage in the central Indian Ocean and shortly after the active stage and during the

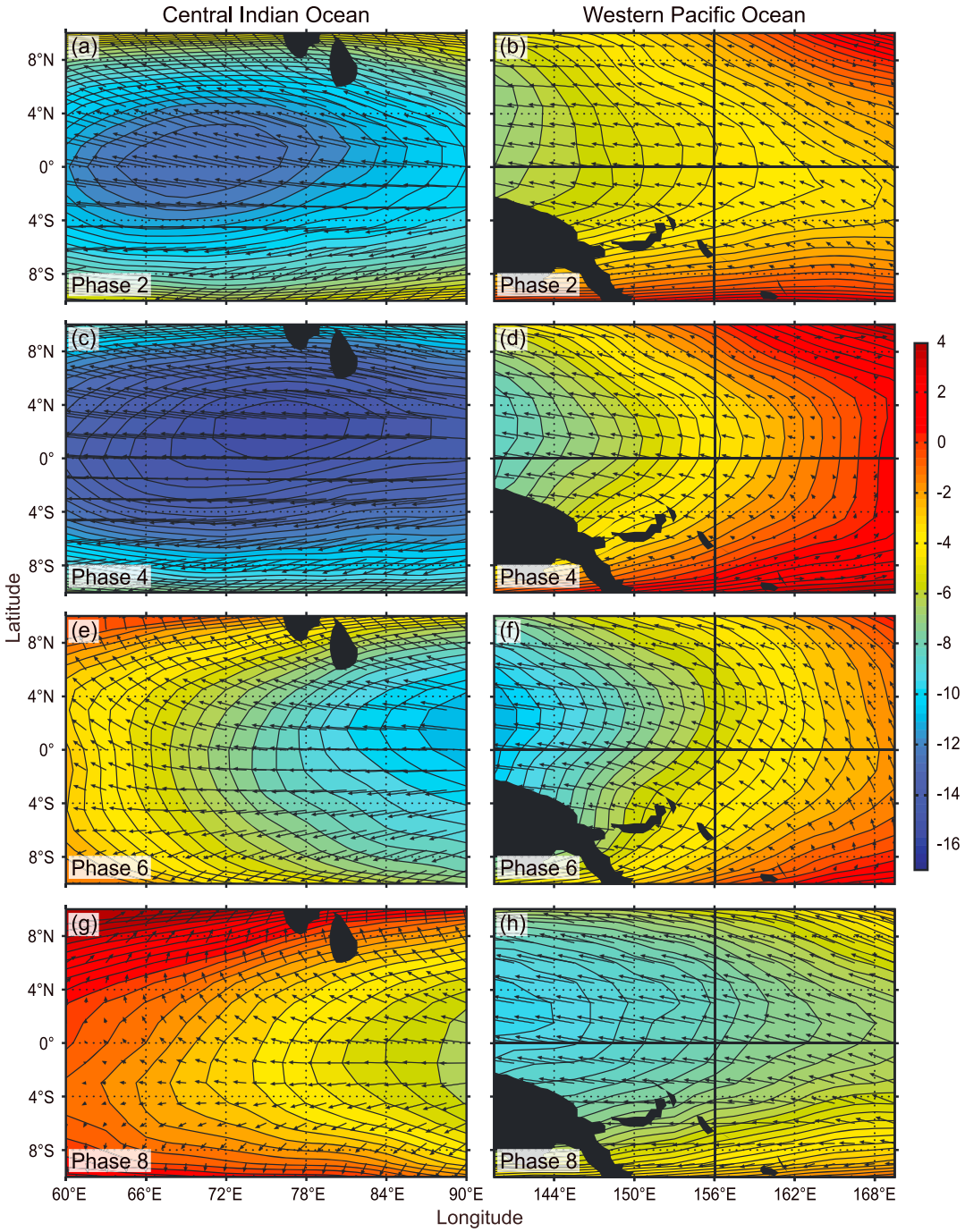


Figure 12. Same as Figure 10 except for the average 200 hPa wind.

beginning of the suppressed stage in the west Pacific Ocean. Below 500 hPa, the winds behave similarly in all regions. In both the central Indian and west Pacific Oceans, the zonal winds below 750 hPa become more westerly (i.e., less easterly) with height, while those between 750 and 500 hPa become more easterly with height, one phase after the BSR peak. Therefore, in the following discussion, we will focus on three vertical wind shear layers: low level (1000–750 hPa), mid-level (750–500 hPa), and upper level (500–200 hPa).

[37] Figure 14 shows maps of the 1000–750 hPa shear in the central Indian Ocean, averaged over all days for which we have analyzed radar data in each phase of the MJO. The 1000–750 hPa shear increases in phases 1–4. Simultaneously, the DCC, WCC, and BSR echoes increase in amount and reach peak occurrence (Figures 7b–7d). The simultaneous rise in deep convection and mesoscale systems with low-level shear might be partially the result of MCS downdrafts transporting mid-level winds to the surface, thus helping to create the surface convergence, vertical motion, and convective initiation required to initiate, maintain, and strengthen MCSs [*Houze*, 1993, 2004]. However, as the active stage in the central Indian Ocean concludes during phase 4, this complementary behavior ceases. Figure 14

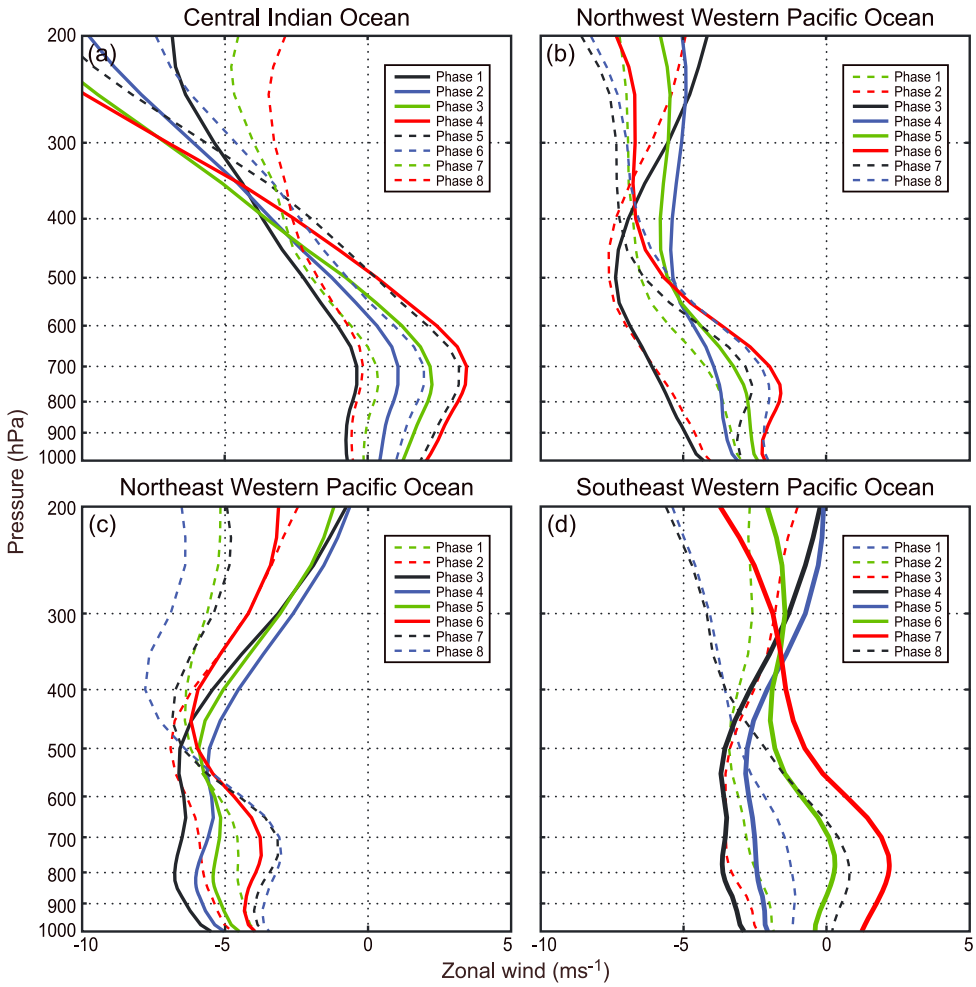


Figure 13. Same as Figure 9 except for zonal wind in m s^{-1}.

shows that large-scale low-level shear maximizes in phase 4, but Figures 7b–7d show a significant decrease in DCC, WCC, and BSR echo coverage. As will be discussed below, we hypothesize that this sudden change in the precipitating cloud population may be related to a dry mid-troposphere and/or acute mid-level shear.

[38] Figure 15 shows that the mid-level (750–500 hPa) shear over the central Indian Ocean is moderately strong in phases 2–3 and begins to become very strong in phase 4, which is one phase after DCC, WCC, and BSR echoes maximize (Figures 7b–7d). Stratiform regions within MCSs are sustained in part by the import of hydrometeors from nearby convective regions of the MCSs and also by mid-level inflow from the environment feeding convergence below the stratiform cloud deck and sustaining the mesoscale downdraft below the cloud deck [*Houze et al.*, 1980; *Houze*, 2004]. A moderate amount of mid-level shear strengthens these effects. However, excessively strong mid-level shear could be detrimental to the MCS, e.g., by separating the lower and upper portions of the stratiform cloud deck or by severing the stratiform region from its associated convective region. Given that the occurrence of BSR echoes peaks prior to the strongest mid-level shear, our results suggest that the variability in BSR echo coverage during the MJO may be influenced positively or negatively by the degree of mid-level shear. Strong mid-level shear might not be as closely related to the decline of the DCC and WCC echoes since these echo entities are less dependent on hydrometeors being transported from another part of the convective system. Instead, the decline of DCC and WCC echoes in phase 4 may be related to the rapid drying of the mid-troposphere seen in Figure 9. The rapid decline in BSR frequency may also be related to this drying. While it is unclear why the large-scale relative humidity, circulation, and vertical wind shear fields change as the MJO passes over a region, our results for the central Indian Ocean suggest that the precipitating cloud population during the active stage of the MJO may be systematically associated with the combined effects of large-scale mid-tropospheric relative humidity, low-level shear, and mid-level shear. The west Pacific Ocean provides the opportunity to investigate these proposed relationships in greater detail since the DCC and WCC peaks during the active stage are temporally isolated from the BSR peak.

[39] The association between the precipitating cloud population during the active stage of the MJO and the large-scale atmospheric conditions throughout most of the west Pacific Ocean appears to be consistent with the relationships observed during the active stage in the central Indian Ocean. Figures 16 and 17 show low- and mid-level shear, respectively, averaged over all days on which we have

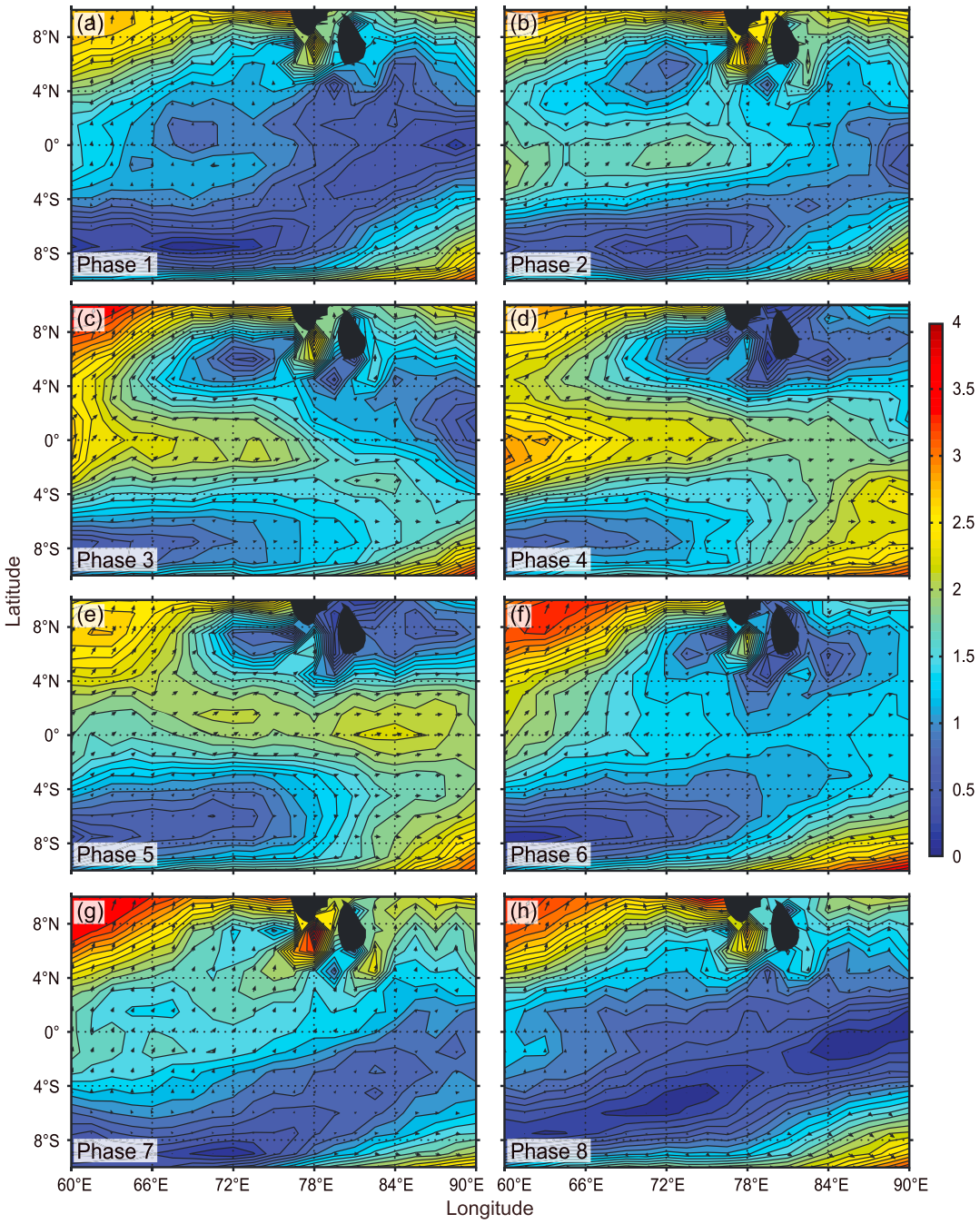


Figure 14. The average direction (vectors) and magnitude (shading) of the 1000–750 hPa shear in the central Indian Ocean for all days during each phase in m s^{-1}.

analyzed TRMM PR data in each phase. During the active stage in the northwestern portion of the west Pacific Ocean, WCC and BSR echoes maximize during phases 6 and 5, respectively (Figures 7g and 7h). Throughout these phases, low-level shear in the northwestern portion of the west Pacific Ocean (Figure 16) is relatively strong and the mid-troposphere is very moist (Figure 9), which suggest that atmospheric conditions may be favorable for WCC and BSR echoes. Thus, the association between low-level shear and the population of mesoscale cloud entities (i.e., WCC and BSR echoes) is consistent in both the central Indian Ocean and northwestern portion of the west Pacific Ocean. However, Figures 14 and 16 indicate that the magnitude of the peak low-level shear is lower than the peak in the central Indian Ocean. While it is unclear why the low-level shear is weaker in the west Pacific Ocean, the sea surface temperature in the west Pacific Ocean is consistently 2–3 K warmer than the central Indian Ocean (not shown), and we suggest that WCCs and BSRs may be able to peak in the west Pacific Ocean with a weaker low-level shear maximum since the conditional instability is greater in this region. Figure 17 indicates that mid-level shear in the northwestern portion of the west Pacific Ocean maximizes during phase 6, which may account for the dramatic reduction in BSR echo

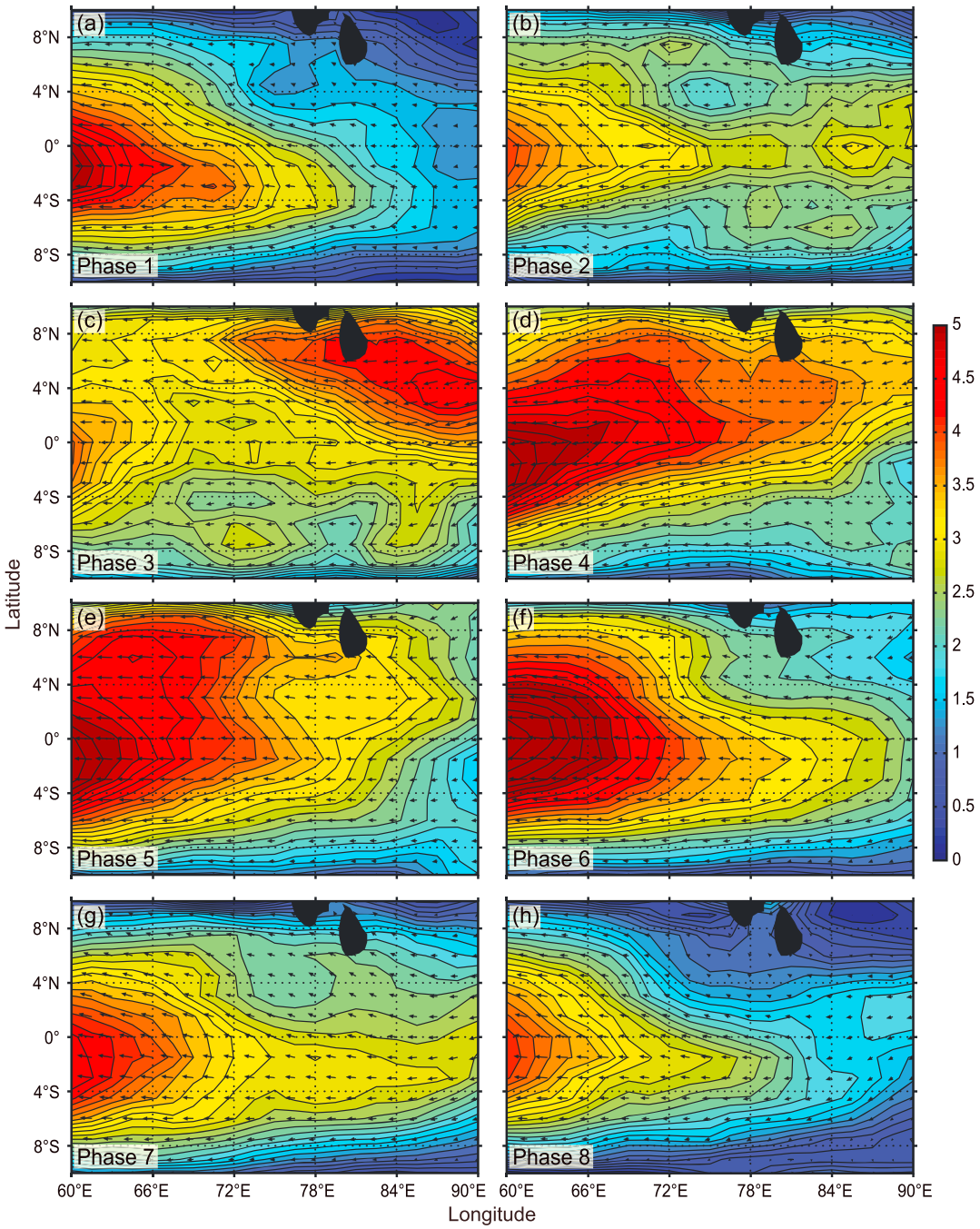


Figure 15. Same as Figure 14 except for 750–500 hPa shear.

frequency during this phase (Figure 7h) since the strong shear might be separating the stratiform regions from their convective sources of hydrometeors. WCCs are most frequent in phase 6 as mid-level shear maximizes (Figure 17). This trend supports the hypothesis that WCCs are less sensitive to mid-level shear than are BSRs since the occurrence of WCCs in the central Indian Ocean peak prior to the peak mid-level shear. Figure 9 indicates that mid-tropospheric relative humidity rapidly declines after phase 6, which corresponds to the statistically significant decrease in WCC echoes in Figure 7c.

[40] WCC and BSR echoes during the active stage of the MJO in the southeastern portion of the west Pacific Ocean are shown in Figures 7n–7p, 9, 16, and 17 to exhibit the same association with large-scale relative humidity, low-level shear, and mid-level shear as WCC and BSR echoes observed during the active stage in the northwestern portion. Additionally, the southeastern portion of the west Pacific Ocean shows that DCC echoes observed during the active stage may occur most frequently when the mid-troposphere is moist and the low-level shear is strong. DCC echoes are shown in Figure 7n to maximize in phase 7, which corresponds to the strongest low-level shear in Figure 16 and the highest mid-tropospheric relative humidity in Figure 9. Given that DCCs in the northeastern portion of the west Pacific Ocean lack a

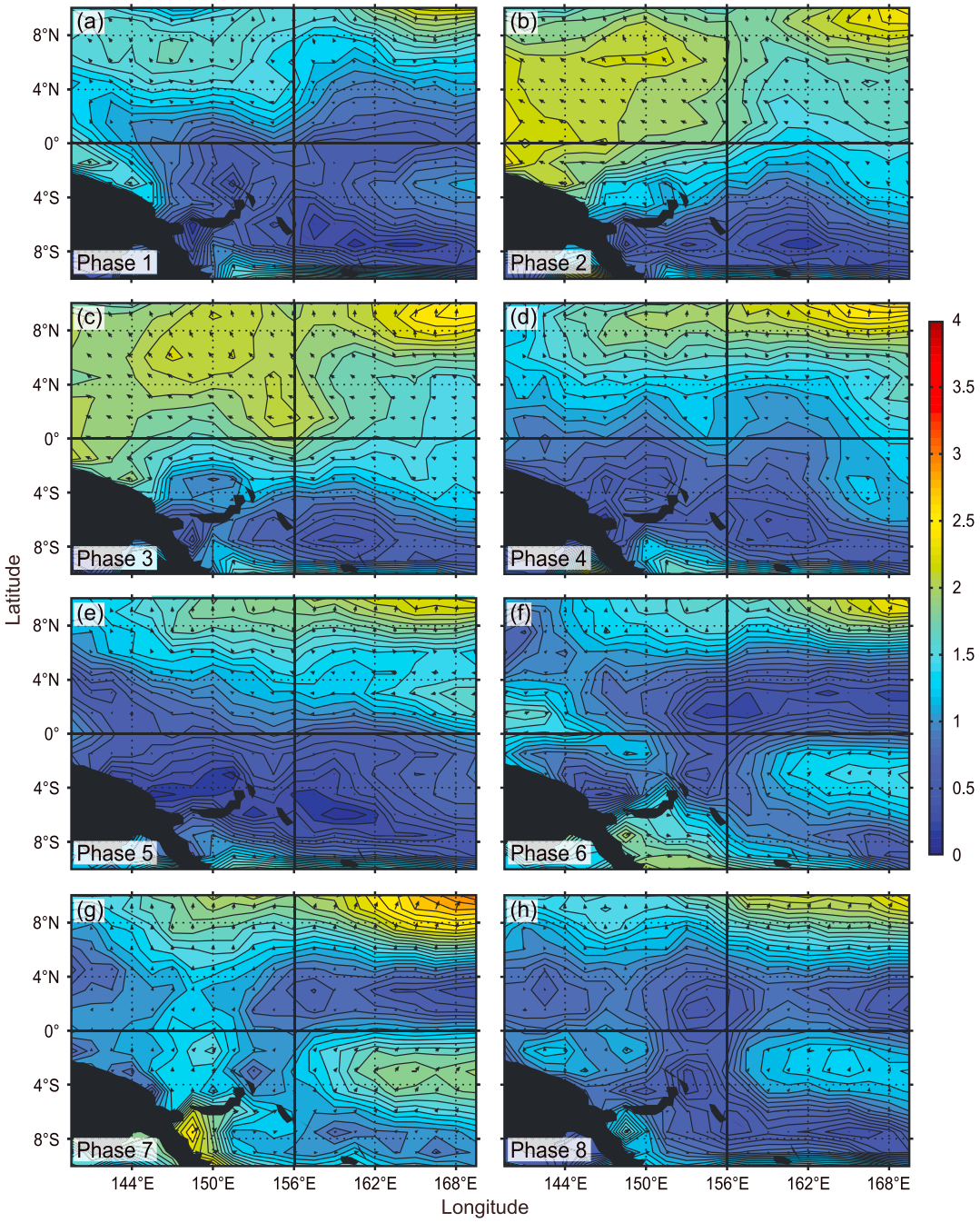


Figure 16. Same as Figure 14 except located in the west Pacific Ocean. The black lines in the west Pacific Ocean show the boundaries of the northwestern, northeastern, and southeastern subregions.

statistically significant peak, the association between DCCs, mid-tropospheric moisture, and low-level shear is not clearly evident in this region.

[41] While we have shown that DCC and WCC echoes observed during the active stage of the MJO in the central Indian Ocean and most of the west Pacific Ocean may be coherently associated with the observed large-scale mid-tropospheric relative humidity and low-level shear, these relationships may not be applicable to the suppressed stage of the MJO. For example, Figure 7b indicates that DCC echoes also peak in the central Indian Ocean during phase 7, which is near the end of the suppressed stage in that region. Phase 7 in the central Indian Ocean is characterized by some of the lowest mid-troposphere relative humidities (Figure 9) and relatively weak low-level shear (Figure 14). A similar trend is observed in the northwestern portion of the west Pacific Ocean when WCC maximizes again in phase 8 (Figures 7g, 9, and 16). Thus, DCCs and WCCs, which represent intense convective updrafts and young or small MCSs, may be able to occur with some frequency when local conditions are sufficiently unstable even if the large-scale vertical wind shear and humidity conditions are unfavorable. However, the BSR peak appears to be consistently associated with a large-scale environment

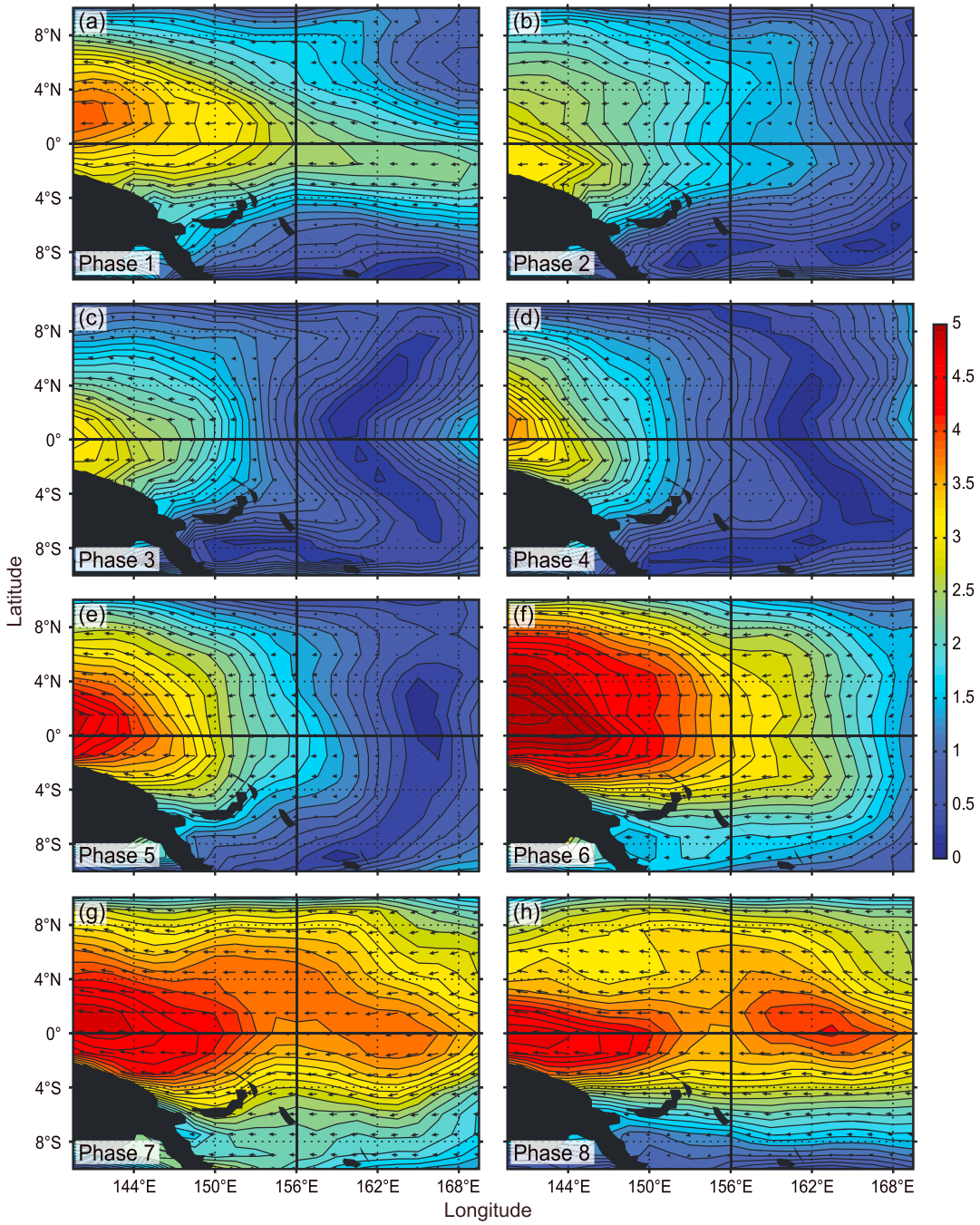


Figure 17. Same as Figure 14 except for 750–500 hPa shear in the west Pacific Ocean. The black lines in the west Pacific Ocean show the boundaries of the northwestern, northeastern, and southeastern subregions.

characterized by a moist mid-troposphere, strong low-level shear, and moderately strong mid-level shear during all phases of the MJO in each geographic region. Thus, BSRs, which represent well-developed MCSs, may require optimal environmental humidity and shear conditions. While these conditions can occur during any phase, we conclude that active phases of the MJO are situations in which these favorable conditions are most common. To some extent, these conditions may be reinforced by feedback from the convection itself.

[42] The association between the precipitating cloud population and large-scale moisture and shear fields during the active stage of the MJO is weakest in the northeastern portion of the west Pacific Ocean. For example, BSR echoes are shown in Figure 7l to broadly maximize in phases 3–7. Figures 9, 16, and 17 indicate that the large-scale mid-upper–level relative humidity, low-level shear, and mid-level shear are highly variable throughout this broad peak in BSR coverage. Given that the MJO tends to manifest its convective coupling in the SPCZ at these longitudes [*Weickmann et al.*, 1985], it should perhaps not be surprising that the relationship between the precipitating cloud population and large-scale relative humidity and vertical wind shear fields is least distinct in this region.

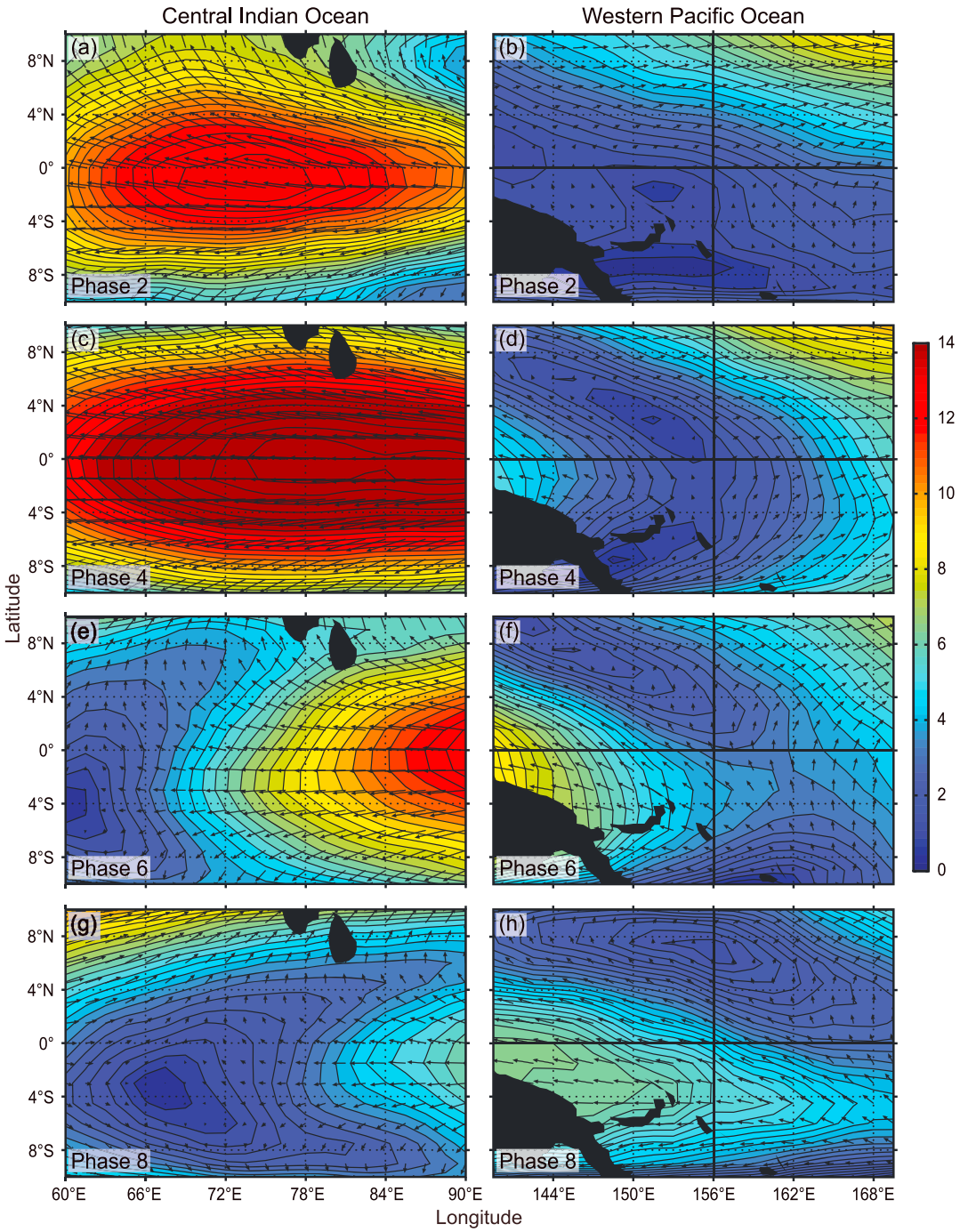


Figure 18. The average direction (vectors) and magnitude (shading) of the 500–200 hPa shear in the central Indian Ocean and west Pacific Ocean for all days during phases 2, 4, 6, and 8 in m s^{-1}. The black lines in the west Pacific Ocean show the boundaries of the northwestern, northeastern, and southeastern subregions.

[43] Mid-tropospheric moisture and low-level shear may also be associated with the ISE maximum in each geographic region. In the central Indian Ocean, ISEs maximize in phase 5, which corresponds to the suppressed stage of the MJO (Figure 7a). Figures 9 and 14 show that the low-level shear is relatively strong and the mid-troposphere is dry during phase 5 in the central Indian Ocean. This pattern of strong 1000–750 hPa shear and dry mid-tropospheric conditions is also observed in each of the west Pacific regions. ISEs do not appear to have a consistent relationship with mid-level shear. ISEs in the central Indian Ocean maximize in phase 5 when the 750–500 hPa shear is strong (Figure 15). However, ISEs in the west Pacific regions maximize in phase 3 (Figures 7e, 7l, and 7m) when the mid-level shear minimizes (Figure 17). ISEs are probably somewhat independent of mid-level shear since most of these shallow echoes likely do not significantly penetrate into the 750–500 hPa layer. If they do, however, they would likely

be inhibited by stronger shear at mid-levels as well as the low mid-level humidity. It is unclear if the large-scale MJO circulation and/or changes in the precipitating cloud population are causing the relatively strong low-level shear and/or dry mid-tropospheric conditions to develop during the suppressed stage of the MJO. Regardless of this question, our analysis indicates that the large-scale environment is favorable to ISE development when these conditions are observed.

[44] Figure 18 shows the upper-level (500–200 hPa) shear in the central Indian and west Pacific Oceans, averaged over all days for which we have analyzed radar data during phases 2, 4, 6, and 8. While the upper-level shear is predominately easterly in both regions, the magnitude of the shear differs vastly between the regions. In the central Indian Ocean, upper-level shear maximizes in phase 4, which is one phase after the BSR peak in Figure 7d. Figure 18c shows that a very large region in the central Indian Ocean is characterized by upper-level shear in excess of $20\,m\,s^{-1}$ at this time. In the northwestern portion of the west Pacific Ocean, upper-level shear peaks in phase 6, and Figure 7p indicates that BSRs peak one phase earlier in phase 5, which is consistent with the central Indian Ocean. However, Figure 18f indicates the maximum upper-level shear in the northwestern portion of the west Pacific Ocean is much weaker than that in the central Indian Ocean, only reaching $9\,m\,s^{-1}$ in an isolated region. A similar pattern is witnessed in the southeastern portion of the west Pacific Ocean. Thus, upper-level shear in the central Indian Ocean and northwestern and southeastern portions of the west Pacific Ocean consistently peaks one phase after BSR echoes, but the peak magnitude greatly differs in the central Indian Ocean and west Pacific regions. The reason for this regional magnitude difference is unclear and requires further research. However, the difference suggests that the upper-level shear may not be an important factor in determining the nature of the precipitating cloud population analyzed by the current study since frequency and variability of the precipitating cloud population is similar in the central Indian and west Pacific Oceans despite these large upper-level shear differences. This result may not be surprising since the structure and dynamics of the precipitating mesoscale features analyzed in the current study tend to be influenced by the low- and mid-level vertical wind shear profile [as discussed by *Moncrieff and Klinker*, 1997; *Houze et al*., 2000; *Mechem et al*., 2006]. These regional differences may suggest that the size and structure of the MCS anvils differ in the central Indian and west Pacific Oceans. However, because of the 17 dBZ sensitivity of the TRMM PR, the anvil structure of MCSs cannot be investigated in the current study.

7. Conclusions

[45] We have used four types of radar echo entities seen in the TRMM PR data to characterize the precipitating cloud population of the MJO. ISEs represent small, shallow precipitating clouds. DCC, WCC, and BSR echoes describe the deepest and widest convective and stratiform components of MCSs. Similar echo entities have been used to understand convective populations in the ITCZ [*Schumacher and Houze*, 2003], the Asian monsoon [*Houze et al*., 2007; *Romatschke et al*,. 2010], and South America [*Romatschke and Houze*, 2010; *Rasmussen and Houze*, 2011]. By examining these radar echo objects over the central Indian and Western Pacific Oceans, we have shown that the areal coverage of each echo feature varies significantly with phase of the MJO. In each of these two regions, ISEs occur most frequently during the suppressed stage, and DCC, WCC, and BSR echoes are most prevalent during the active stage. Previous studies have used OLR and brightness temperature in MJO settings to show that the sizes of mesoscale systems in the cloud population vary [*Chen et al*., 1996; *Houze et al*., 2000; *Benedict and Randall*, 2007; *Yuan and Houze*, 2012]. The TRMM PR enables us now to determine how the makeup of the convective population varies from one part of the MJO to another in more specific terms. The TRMM PR data allow us to identify four fundamentally different types of convective and mesoscale entities within the precipitating cloud population and to produce a census of these entities that shows how their relative numbers vary with phase of the MJO.

[46] In this paper, we have carried out this census over the region of the central Indian Ocean, where the MJO convective coupling initiates, and over the west Pacific region, which is traversed by the propagating MJO disturbance. By using 14 boreal winter seasons of TRMM PR data from 1998–2011, this study provides a robust climatology of the precipitating cloud population elements during each phase of the MJO in the central Indian and west Pacific Oceans. These results can be used to verify numerical models and assess if conditions observed during field campaigns such as TOGA-COARE, the *Mirai* Indian Ocean cruise for study of the MJO-convection Onset (MISMO), and the Dynamics of the Madden-Julian Oscillation/ARM MJO Investigation Experiment/Cooperative Indian Ocean experiment on the Intraseasonal Oscillation in the Year 2011 (DYNAMO/AMIE/CINDY-2011) are representative of climatological conditions.

[47] Regardless of geographic region and phase of the MJO, we find that:

[48] 1. ISEs are always present and are especially concentrated within the ITCZ portions of each oceanic region. In terms of number, ISEs are the most frequently occurring entities of the precipitating cloud population at all times. They are the most variable component of the precipitating cloud population in terms of number and tend to maximize during the convectively suppressed stage of the MJO.

[49] 2. BSR echoes, which occur in connection with well-developed MCSs, dominate the variability of the precipitating cloud population in terms of areal coverage and are most prevalent during the active stage of the MJO, when they dominate the area covered by precipitation.

[50] 3. DCC and WCC echoes also maximize in occurrence during the active stage and are more frequent and variable than BSR echoes in terms of number. DCCs represent the most vigorous convective updrafts and WCCs are closely associated with young or small MCSs.

[51] While the variability of each echo entity has a similar magnitude in the central Indian Ocean and west Pacific regions, subtle differences in the convective population exist between the regions:

[52] 1. Over the central Indian Ocean, the spatial distribution of echoes is relatively homogeneous, WCC echoes are numerically more common than DCC echoes, and ISEs peak in occurrence at the beginning of the suppressed stage of the MJO. A simultaneous peak in DCC, WCC, and BSR echoes characterizes the active stage of the MJO, which

suggests that the precipitating cloud population of the active phase contains convective cells and MCSs of all sizes and maturations.

[53] 2. In the west Pacific, the spatial distribution of echoes is inhomogeneous with DCC, WCC, and BSR echoes preferentially occurring along a diagonal from the warm pool in the northwestern portion to the South Pacific Convergence Zone in the southeastern portion. DCC echoes are numerically more frequent than WCC echoes. ISEs peak in occurrence at the end of the suppressed stage.

[54] 3. During the active stage in the northwestern portion of the west Pacific and southeastern portion of the west Pacific Ocean, BSR echoes maximize in frequency one phase before WCC echoes, which suggests that extremely large MCSs are more common at the beginning of the active stage and smaller or shrinking MCSs are more common as the active stage concludes.

[55] 4. The northeastern portion of the west Pacific Ocean displays little systematic variability with phase of the MJO, probably because the MJO disturbance tends to plunge southward into the SPCZ region in these longitudes.

[56] ERA-interim reanalysis fields composited for the time period of TRMM PR data analyzed herein show how the frequency of occurrence of the four types of echo entities vary in relation to large-scale vertical wind shear and humidity:

[57] 1. ISEs are profusely present in all phases of the MJO in both the central Indian and west Pacific Oceans. However, they maximize during the suppressed stage when the mid-troposphere is driest and the low-level shear is relatively strong. This maximum in ISE occurrence during the suppressed stage is, moreover, not simply related to having more echo-free space available for ISE development.

[58] 2. DCC echoes in the central Indian Ocean and southeastern portion of the west Pacific Ocean occur most frequently during the MJO active stage, when the large-scale low-level (1000–750 hPa) shear is relatively strong and the mid-troposphere is relatively moist. A statistically significant DCC peak does not occur in the northwestern portion of the west Pacific Ocean, and there is no coherent relationship between DCC, mid-tropospheric moisture, and low-level shear in the northeastern portion of the west Pacific Ocean.

[59] 3. WCC echoes appear to be most prevalent during the active MJO stage, when large-scale low-level (1000–750 hPa) shear is strong and the mid-troposphere is moist. When low-level shear is enhanced, momentum transport by MCS downdrafts may create more robust surface convergence and convective initiation during the active stage.

[60] 4. BSR echoes preferentially occur when a moderate amount of large-scale mid-level (750–500 hPa) shear occurs within a moist mid-troposphere that has strong low-level (1000–750 hPa) shear. The strong low-level shear may aid in initiating the convection required to sustain the convective moisture source of the BSRs, and moderately strong mid-level shear may help the deep convection develop mesoscale organization. However, we suggest that excessively strong mid-level shear may disconnect the stratiform region from its convective moisture source. This separation would account for the rapid decline in BSR frequency at the end of the active stage. While strong mid-level shear has been associated with stratiform convection in numerous studies [e.g., *Saxen and Rutledge*, 2000], the literature has not formally stated whether too much mid-level shear could be inimical to mesoscale organization. Evidence in support of a deep shear threshold may, however, be found in previous studies. For example, *Lin and Johnson* [1996] showed that the maximum in 700–150 hPa shear lags the precipitation maximum by 5–10 days, which is consistent with our maximum in 750–500 hPa shear and 500–200 hPa shear lagging the BSR peak by one phase. If very strong mid-level shear is shown to be detrimental to MCSs, while moderate shear is helpful, the changing wind profile associated with a developing or propagating MJO could greatly influence the nature of the convective coupling since the heating feedback of large, organized mesoscale systems is notably more top heavy [*Houze*, 1982, 1989, 2004]. The northeastern portion of the west Pacific Ocean, which the MJO often avoids in favor of the warm waters in the SPCZ, lacks a coherent association between mid-level shear and BSR echoes.

[61] The associations discussed above contribute to understanding why DCC, WCC, and BSR echoes simultaneously maximize in the central Indian Ocean but BSR echoes maximize one phase before DCC and WCC echoes over most of the west Pacific Ocean (Figure 7). Low- and mid-level shear maximize one phase after the BSR peak in both regions. However, mid-tropospheric relative humidity dramatically decreases one phase after the BSR peak in the central Indian Ocean but does not dramatically decrease until two phases after the BSR peak in the west Pacific Ocean. Thus, the delayed DCC and WCC peak in most of the west Pacific Ocean might be associated with the mid-troposphere remaining moist for a longer period of time in these regions. The reason for the persistent mid-upper tropospheric moisture is unknown and remains a question for further research.

[62] Averages of all ocean grid boxes in the ERA-interim reanalysis suggest that large-scale conditions are uniformly moist below 800 hPa regardless of the presence of ISEs or deep convective entities, phase of the MJO, or geographic region. Similar to *Yuan and Houze* [2012], we find that within the MJO, the primary variation of the moisture content occurs in the mid-upper levels of the troposphere. The central Indian Ocean and the portions of the west Pacific Ocean most affected by the MJO are characterized by an increase in mid-tropospheric moisture one phase prior to a statistically significant rise in DCC, WCC, and BSR echoes. This moistening prior to the onset of deep convection is consistent with a numerous previous studies such as *Lin and Johnson* [1996] and *Kiladis et al*. [2005]. The moisture in the mid-troposphere is greatest as DCC, WCC, and BSR echoes maximize during the active stage. Substantial drying appears to occur in concert with a significant decline in the frequency of WCC and BSR echoes.

[63] While this study suggests that systematic associations exist among the precipitating cloud population and the large-scale relative humidity, circulation, and vertical wind shear fields, it is, of course, unclear if the precipitating cloud population is causing or reacting to large-scale conditions, or—perhaps more likely—both. The moistening prior to the onset of deep, mesoscale convection has been theorized to result from planetary wave–induced vertical motion [e.g., *Hendon and Salby*, 1994], horizontal advection [e.g., *Tromeur and Rossow*, 2010], and/or accumulation from convective bursts occurring at shorter time scales [e.g., *Benedict and Randall*, 2007]. *Yuan and Houze* [2012] also found that mid-tropospheric moisture

varies in concert with large, mature MCSs and encountered the same attribution difficulty. Their study suggests that MCSs in the active stage are initially a reaction to an increase in the large-scale mid-tropospheric moisture from either nonlocal advection or accumulation from previous convection. This conclusion is based on observations of elevated mid-tropospheric moisture during the active stage of the MJO regardless of the presence of deep convection. *Yuan and Houze* [2012] also suggested that after the initial MCS increase during the active stage, mesoscale convection acts as a positive feedback for mid-tropospheric moisture. While the large-scale circulation associated with the MJO may be a factor contributing to the slow rise in mid-tropospheric moisture in the active MJO phase, we suggest that the mesoscale population likely contributes to the large-scale moisture field to some degree since *Zelinka and Hartmann* [2009] suggest that the deep convective population can moisten the mid-upper troposphere over a region larger than a single convective entity. The results of the current study are consistent with the two hypotheses of *Yuan and Houze* [2012]. DCC, WCC, and BSR may first be a reaction to mid-tropospheric moisture since the mid-troposphere moistens prior to a statistically significant rise in DCC, WCC, and BSR echoes. Then, mid-tropospheric moisture continues to slowly rise as DCC, WCC, and BSRs significantly increase, which would be consistent with (but not prove) the positive moisture-convection feedback hypothesis. The present study expands the hypotheses of *Yuan and Houze* [2012] by highlighting how the occurrence of deep convective entities in the MJO is related to the interplay of mid-level moistening and large-scale shear at low and middle levels. Specifically, we suggest that a large-scale environment with strong low-level shear, moderate mid-level shear, and a moist mid-upper troposphere is favorable to the extremely large mesoscale convective systems that produce BSRs, which dominate the areal variability of the precipitating cloud population and drive the heating profile toward a top-heavy configuration.

[64] While our results are consistent with and expand upon previous studies such as *Yuan and Houze* [2012], how the large-scale MJO circulation and/or cloud population cause changes in the large-scale moisture and shear field remains unknown. Observational studies can suggest hypotheses concerning the association between the precipitating cloud population and large-scale environment. However, numerical modeling studies could more decisively establish the likely interactive physical connections linking the precipitating cloud population with the large-scale humidity, circulation, and vertical wind shear fields in the MJO, provided the models produce relationships of the type seen herein in the TRMM PR data and ERA-interim reanalysis fields.

[65] Field experiments may also help establish these connections. The DYNAMO/AMIE/CINDY campaigns provide a unique opportunity to compare the composites presented in the current study with three individual MJO events that occurred over the central Indian Ocean from 1 October 2011 to 15 January 2012 using dual polarimetric SPolKa radar and rawinsonde data on Addu Atoll (0.6°S, 73.1°E). The evolutionary sequence of the precipitating cloud population observed during DYNAMO/AMIE is quite similar to that seen in the composites presented in the current study. However, as *Zuluaga and Houze* [2013] have shown, the precipitation that occurs during active phases is relatively short bursts of 2–4 days, with cloud population undergoing a sequence of shall convection, to DCCs, to WCCs, to BSRs similar to that which we see on the MJO scale but on a time scale shorter than that on the MJO phase. *Powell and Houze* [2013] also analyzed SPolKa S-band radar and showed that the stratiform precipitation dominates the variability of the precipitating cloud population by areal coverage. Additionally, they found that the depth of the moisture layer rapidly builds up from middle to upper levels in the 3–6 days preceding the active stage of the MJO. The current study has also found the mid-troposphere (800–500 hPa) moistening prior to the stage dominated by BSRs, but this moistening occurs over one to two phases (~1–2 weeks). Thus, these studies have a similar overall pattern of the large-scale relative humidity variability, but the time scales of the variability differ, which likely is attributable to the smoothing that results from the compositing that we have had to do by phase of the MJO for the 14 year TRMM PR data set. For example, significant moistening may occur during a phase that lasted 10 days but that moistening may have been concentrated over a few days rather than spread uniformly over 10 days. Thus, while the magnitude and time scale of variability observed in our 14 year composites may differ from the intermittent concentrated bursts of precipitation in the active phases of MJO events, we are confident that the variability in the precipitating cloud population and its association with observed large-scale environment described in the current study is qualitatively representative of these events expressed on the MJO time scale.

[66] **Acknowledgment**s. The authors would like to thank Stacy Brodzik for initiating this study, Manuel Zuluaga for downloading and converting the ERA-interim reanalysis, Scott Powell for helpful comments on the manuscript, and Beth Tully for improving the graphics. Additionally, the authors would like to thank the three anonymous reviewers who provided informative and helpful comments on the manuscript. ERA-interim reanalysis was provided by the European Centre for Medium-Range Weather Forecasts. This research is sponsored by the Department of Energy grants DE-SC0001164/ER-64752 and DE-SC0008452, the DYNAMO–National Science Foundation grant AGS-1059611, and the Precipitation Measuring Mission–National Aeronautics and Space Administration (PMM-NASA) grant NNX10AH70G.

References

Awaka, J., T. Iguchi, H. Kumagai, and K. Okamoto (1997), Rain type classification algorithm for TRMM Precipitation Radar, paper presented at Proc. 1997 Int. Geoscience and Remote Sensing Symp. (IGARSS '97)—*Remote Sensing: A Scientific Vision for Sustainable Development,* Singapore, IEEE, 4(6), 1633–1635.

Benedict, J. J., and D. A. Randall (2007), Observed characteristics of the MJO relative to maximum rainfall, *J. Atmos. Sci.*, *64*(7), 2332–2354.

Benedict, J.J., and D. A. Randall (2009), Structure of the Madden-Julian Oscillation in the superparameterized CAM, *J. Atmos. Sci.*, *66*(11), 3277–3296.

Bladé, I., and D. L. Hartmann (1993), Tropical intraseasonal oscillations in a simple nonlinear model, *J. Atmos. Sci.*, *50*(17), 2922–2939.

Dee, D. P., et al. (2011), The ERA-Interim reanalysis: Configuration and performance of the data assimilation system, *Q. J. R. Meteorol. Soc.*, *137*(656), 553–597.

Del Genio, A. D., Y. Chen, D. Kim, and MS Yao (2012), The MJO transition from shallow to deep convection in *CloudSat*/CALIPSO data and GISS GCM simulations, *J. Clim.*, *25*(11), 3755–3770.

DeMott, C. A., and S. A. Rutledge (1998), The vertical structure of TOGA COARE convection. Part I: Radar echo distributions, *J. Atmos. Sci.*, *55*(17), 2730–2747.

Chen, S. S., R. A. Houze, Jr., and B. E. Mapes (1996), Multiscale variability of deep convection in relation to large-scale circulation in TOGA COARE, *J. Atmos. Sci.*, *53*(10), 1380–1409.

Cheng, C.-P., and R. A. Houze Jr. (1979), The distribution of convective and mesoscale precipitation in GATE radar echo patterns, *Mon. Weather Rev.*, *107*(10), 1370–1381.

Gill, A. E. (1980), Some simple solution for heating-induced tropical circulation, *Q. J. R. Meteorol. Soc.*, *106*(449), 447–462.

Haertel, P. T., G. N. Kiladis, A. Denno, and T. M. Rickenbach (2008), Vertical-mode decompositions of 2-day waves and the Madden-Julian Oscillation, *J. Atmos. Sci.*, *65*(3), 813–833.

Hendon, H. H., and M. L. Salby (1994), The life-cycle of the Madden-Julian Oscillation, *J. Atmos. Sci.*, *51*(15), 2225–2237.

Houze, R. A., Jr., and C.-P. Cheng (1977), Radar characteristics of tropical convection observed during GATE: Mean properties and trends over the summer season, *Mon. Weather Rev.*, *105*(8), 964–980.

Houze, R. A., Jr., C.-P. Cheng, C. A. Leary, and J. F. Gamache (1980), Diagnosis of cloud mass and heat fluxes from radar and synoptic data, *J. Atmos. Sci.*, *37*(4), 754–773.

Houze, R. A., Jr. (1982), Cloud clusters and large-scale vertical motions in the tropics, *J. Meteorol. Soc. Jpn.*, *60*(1), 396–410.

Houze, R. A., Jr. (1989), Observed structure of mesoscale convective systems and implications for large-scale heating, *Q. J. R. Meteorol. Soc.*, *115*(487), 425–461.

Houze, R. A., Jr. (1993), *Cloud Dynamics*, 573 pp., Academic Press, San Diego, Calif.

Houze, R. A., Jr., S. S. Chen, D. E. Kingsmill, Y. Serra, and S. E. Yuter (2000), Convection over the Pacific warm pool in relation to the atmospheric Kelvin-Rossby wave, *J. Atmos. Sci.*, *57*(18), 3058–3089.

Houze, R. A., Jr. (2004), Mesoscale convective system, *Rev. Geophys.*, *2004*, RG4003, doi:10.1029/2004RG000150.

Houze, R. A., Jr., D. C. Wilton, and B. F. Smull (2007), Monsoon convection in the Himalayan region as seen by the TRMM precipitation, *Mon. Weather Rev.*, *133*(627), 1389–1411.

Iguchi, T., R. Meneghini, J. Awaka, T. Kozu, and K. Okamoto (2000a), Rain-profiling algorithm for TRMM Precipitation Radar data, *Adv. Space Res.*, *25*(5), 973–976.

Iguchi, T., T. Kozu, R. Meneghini, J. Awaka, and K. Okamoto (2000b), Rain-profiling algorithm for the TRMM Precipitation Radar, *J. Appl. Meteorol.*, *39*(12), 2038–2052.

Kiladis, G. N., K. H. Straub, and P. T. Haertel (2005), Zonal and vertical structure of the Madden-Julian oscillation, *J. Atmos. Sci.*, *62*(8), 2790–2809.

Kingsmill, D. E., and R. A. Houze, Jr. (1999), Kinematic characteristics of air flowing into and out of precipitating convection over the west Pacific warm pool: An airborne Doppler radar survey, *Q. J. R. Meteorol. Soc.*, *125*(556), 1165–1207.

Kummerow, C., W. Barnes, T. Kozu, J. Shiue, and J. Simpson (1998), The Tropical Rainfall Measuring Mission (TRMM) sensor package, *J. Atmos. Oceanic Technol.*, *15*(3), 809–817.

Lau, K.-M., L. Peng, C. H. Sui, T. Nakazawa (1989), Dynamics of super cloud clusters, westerly wind bursts, 30-60 day oscillation and ENSO: An unified view, *J. Meteorol. Soc. Jpn.*, *67*(2), 205–219.

Lau, K.-M., and H.-T., Wu (2010), Characteristics of precipitation, cloud, and latent heating associated with the Madden-Julian Oscillation, *J. Clim.*, *23*(3), 504–518.

Lin, J., B. Mapes, M. Zhang, and M. Newmann (2004), Stratiform precipitation, vertical heating profiles, and the Madden–Julian Oscillation, *J. Atmos. Sci.*, *61*(3), 296–309.

Lin, X., and R. H. Johnson (1996), Kinematic and thermodynamic characteristics of the flow over the western Pacific warm pool during TOGA COARE, *J. Atmos. Sci.*, *53*(22), 695–715.

Lindzen, R. S. (1974), Wave-CISK in the tropics, *J. Atmos. Sci.*, *31*(1), 156–179.

Madden, R. A. (1986), Seasonal variations of the 40-50 day oscillation in the tropics, *J. Atmos. Sci.*, *43*(24), 3138–3158.

Madden, R. A., and P. R. Julian (1971), Detection of a 40-50 day oscillation in the zonal wind in the tropical Pacific, *J. Atmos. Sci.*, *28*(8), 702–708.

Madden, R. A., and P. R. Julian (1972), Description of global-scale circulation cells in the tropics with a 40-50 day period, *J. Atmos. Sci.*, *29*(5), 1109–1123.

Mapes, B. E., and R. A. Houze Jr. (1993), Cloud clusters and superclusters over the oceanic warm pool, *Mon. Weather Rev.*, *121*(5), 1398–1415.

Mechem, D. B., S. S. Chen, and R. A. Houze (2006), Momentum transport processes in the stratiform regions of mesoscale convective systems over western Pacific warm pool, *Q. J. R. Meteorol. Soc.*, *132*(616), 709–732.

Miura, H., M. Satoh, T. Nasuno, A. T. Noda, and K. Oouchi (2007), A Madden-Jullian Oscillation event realistically simulated by a global cloud resolving model, *Science*, *318*(5857), 1763–1765.

Miyakawa, T., Y. N. Takayabu, T. Nasuno, H. Miura, M. Satoh, and M. W. Moncrieff (2012), Convective momentum transport by rainbands within a Madden-Julian Oscillation in a global nonhydrostatic model with explicit deep convective processes. Part 1: Methodology and general results, *J. Atmos. Sci.*, *69*(4), 137–1338.

Moncrieff, M. W., and E. Klinker (1997), Organized convective systems in the tropical western Pacific as a process in general circulation models: A TOGA-COARE case-study, *Q. J. R. Meteorol. Soc.*, *123*(540), 805–827.

Morita, J., Y. N. Takayabu, S. Shige, and Y. Kodama (2006), Analysis of rainfall characteristics of the Madden-Julian Oscillation using TRMM satellite data, *Dyn. Atmos. Oceans*, *42*, 107–126, doi:10.1016/j.dynatmoce.2006.02.002.

Powell, S. W., and R. A. Houze Jr. (2013), The cloud population and onset of the Madden-Julian Oscillation over the Indian Ocean during DYNAMO-AMIE, *J. Atmos. Sci.*, submitted.

Saxen, T. R., and S. A. Rutledge (2000), Surface rainfall-cold cloud fractional coverage relationship in TOGA COARE: A function of vertical wind shear, *Mon. Weather Rev.*, *128*(2), 407–415.

Schumacher, C., and R. A. Houze Jr. (2003), The TRMM Precipitation Radar's view of shallow, isolated rain, *J. Appl. Meteorol.*, *42*(10), 1519–1524.

Sperber, K. R., (2003), Propagation and the vertical structure of the Madden-Julian Oscillation, *Mon. Weather Rev.*, *131*(12), 3018–3037.

Stephens, G. L., P. J. Webster, R. H. Johnson, R. Engelen, and T. L'Ecuyer (2004), Observational evidence for the mutual regulation of the tropical hydrological cycle and tropical sea surface temperatures, *J. Clim.*, *17*(11), 2213–2224.

Straub, K.H. (2012), MJO initiation in the realtime multivariate MJO index. *J. Clim.*, doi:http://dx.doi.org/10.1175/JCLI-D-12-00074.1.

Randall, D., M. Khairoutidinov, A. Arkawa, and W. Grabowski (2003), Breaking the cloud parameterization deadlock, *Bull. Am. Meteorol. Soc.*, *84*(11), 1547–1564.

Riley, E. M., B. E. Mapes, and S. N. Tulich (2011), Clouds associated with the Madden-Julian Oscillation: A new perspective from CloudSat, *J. Atmos. Sci.*, *68*(12), 3032–3051.

Rasmussen, K.L., and R. A. Houze Jr. (2011), Orogenic convection in subtropical South America as seen by the TRMM PR, *Mon. Weather Rev.*, *139*(8), 2399–2420.

Romatschke, U., and R. A. Houze Jr. (2010), Extreme summer convection in South America, *J. Clim.*, *23*(14), 3761–3791.

Romatschke, U., S. Medina, and R. A. Houze Jr. (2010), Regional, seasonal, and diurnal variations of extreme convection in the South Asian region, *J. Clim.*, *23*(2), 419–439.

Roundy, P. E., C. J. Schreck, and M. A. Janiga (2009), Contributions of convectively coupled equatorial Rossby waves and Kelvin waves to the real-time multivariate MJO indices, *Mon. Weather Rev.*, *137*(1), 469–478.

Takioka, T., K. Yamazaki, A. Kitoh, and T. Ose (1988), The equatorial 30-60 day oscillation and the Arakawa-Schubert penetrative cumulus parameterization, *J. Meteorol. Soc. Jpn.*, *66*(6), 883–901.

Tian, B., D. E. Waliser, E. J. Fetzer, and Y. L. Yung (2010), Vertical moist thermodynamic structure of the Madden-Julian Oscillation in atmospheric infrared sounder retrievals: An update and a comparison to ECMWF interim re-analysis, *Mon. Weather Rev.*, *138*(12), 4576 –4582.

Tromeur, E., and W. B. Rossow (2010), Interaction of tropical deep convection with the large-scale circulation of the MJO, *J. Clim.*, *23*(7), 1837–1853.

Vincent, D. G. (1994), The South-Pacific Convergence Zone (SPCZ)—A review, *Mon. Weather Rev.*, *122*(9), 1949–1970.

Weickmann, K. M., G. R. Lussky, and J. E. Kutzbach (1985), Intraseasonal (30-60 day) fluctuations of outgoing longwave radiation and 250-mb streamfunction during northern winter, *Mon. Weather Rev.*, *113*(6), 941–961.

Wheeler, M. C., and H. H. Hendon (2004), An all-season real-time multivariate MJO index: Development of an index for monitoring and prediction, *Mon. Weather Rev.*, *132*(8), 1917–1932.

Wu, Z. (2003), A shallow CISK, deep equilibrium mechanism for the interaction between large-scale convection and large-scale circulations in the tropics. *J. Atmos. Sci.*, *60*(2), 377–392.

Yuan, J., and R. A. Houze Jr. (2010), Global variability of mesoscale convective system anvil structure from A-train satellite data, *J. Clim.*, *23*(21), 5864–5888.

Yuan, J., and R. A. Houze Jr. (2012), Deep convective systems observed by A-Train in the tropical Indo-Pacific region affected by the MJO, *J. Atmos. Sci.*, *70*(2), 465–486.

Yuter, S E., and R. A. Houze Jr. (1998), The natural variability of precipitating clouds over the western Pacific warm pool, *Q. J. R. Meteorol. Soc.*, *124*(545), 53–99.

Zelinka, M. D., and D. L. Hartmann (2009), Response of humidity and clouds to tropical deep convection. *J. Clim.*, *22*(9), 2389–2404.

Zhang, C. (2005), Madden-Julian Oscillation, *Rev. Geophys.*, *43*, RG2003, doi:10.1029/2004RG000158.

Zhang, G. J., and X. Song (2009), Interaction of deep and shallow convection is key to Madden-Julian Oscillation simulation, *Geophys. Res. Lett.*, *36*, 9708, doi:10.1029/2009GL037340.

Zuluaga, M. D., and R. A. Houze, Jr. (2013), Evolution of the population of precipitating convective systems over the Equatorial Indian Ocean in active phases of the Madden-Julian Oscillation. *J. Atmos. Sci.*, submitted.